# **ARTICLE**

# **Principle and Applications of Peak Force Infrared Microscopy**

Le Wang, a+ Haomin Wang a+ and Xiaoji G. Xu \*a

Received 00th January 20xx, Accepted 00th January 20xx

DOI: 10.1039/x0xx00000x

The peak force infrared (PFIR) microscopy is an emerging atomic force microscopy (AFM)-based infrared microscopy that bypasses Abbe's diffraction limit on spatial resolution. The PFIR microscopy utilizes a nanoscopically sharp AFM tip to mechanically detect the tip-enhanced infrared photothermal response of the sample in the time domain. The time-gated mechanical signals of cantilever deflections transduce the infrared absorption of the sample, delivering infrared imaging and spectroscopy capability at sub 10 nm spatial resolution. Both infrared absorption response and mechanical properties of the sample are obtained in parallel while preserving the surface integrity of the sample. This review describes the constructions of the PFIR microscope and several variations, including multiple pulse excitation, total internal reflection geometry, dual-color configuration, liquid-phase operations, and integrations with simultaneous surface potential measurement. Representative applications of PFIR microscopy are also included in this review. In the outlook section, we lay out several future directions of innovations in PFIR microscopy and applications in chemical and material research.

#### **Key learning points**

- (1) Limits of traditional IR microscopy and needs for a higher spatial resolution.
- (2) Mechanism and instrumentation of peak force infrared microscopy that accesses IR information at the nanoscale.
- (3) Key concepts and elements included in the development of peak force infrared microscopy.
- (4) Applications of peak force infrared microscopy in organic, inorganic, and biological materials in air and liquid conditions.

### 1. Introduction

Infrared (IR) radiation directly couples to the vibrational modes of functional groups. The characteristic IR absorptions by chemical bonds provide a route for label-free and non-invasive chemical identification. A chemical distribution map can be constructed based on heterogeneous IR absorptions by scanning sample areas with IR illumination. However, traditional IR microscopy is restricted by Abbe's diffraction limit ( $\sim \lambda/2$ ), and is unable to reach nanoscale spatial resolution with conventional far-field configurations. As the research frontier of chemistry increasingly involves the identification and utilization of materials and molecules at the nanoscale,2 the spatial resolution of IR microscopy needs to be significantly improved. A general approach to bypass the diffraction limit of IR microscopy is through the integration of atomic force microscopy (AFM). This approach can be established in two different ways: one way is to utilize the near-field scattering by the nanoscopic AFM tip and perform optical detection, which leads to the method of scattering scanning near-field optical microscopy (s-SNOM).3 In s-SNOM, the IR field can be localized and enhanced to the tip apex with a metallic AFM tip, which creates a sub-diffraction limit excitation volume.4 Another increasingly popular route is to perform mechanical detection on the photothermal response of the sample upon the illumination by IR radiations, which leads to a category of AFM-IR.5 In the case of s-SNOM, scattered light from the tip-sample

region is collected and measured. In contrast, AFM-IR leverages the high mechanical sensitivity of the uncoated or metal-coated AFM cantilever to measure the photothermal mechanical response of the sample induced by IR absorptions. The early concept of AFM mechanical detection of IR absorption was demonstrated by Mark Anderson in 2000.<sup>6</sup> Since the invention of photothermal induced resonance (PTIR) with the contact mode AFM by Alexandre Dazzi in 2005,<sup>7</sup> AFM-IR methods quickly gained popularity in chemical nanoimaging and spectroscopy.<sup>5,8</sup> Emerging methods include Resonance-Enhanced Infrared Nanospectroscopy (REINS)<sup>9</sup> or resonance-enhanced AFM-IR, and photo-induced force microscopy (PiFM) and/or tapping mode AFM-IR,<sup>10</sup> have accelerated the development

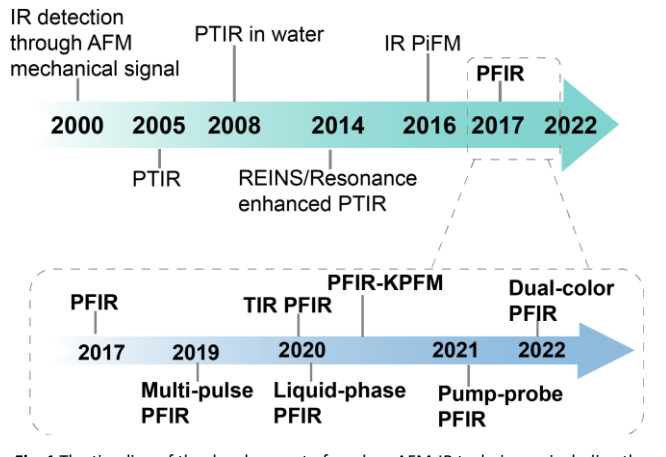


**Fig. 1** The timeline of the development of modern AFM-IR techniques, including the variants of the PFIR microscopy. The time of techniques is sorted according to publication dates.

<sup>&</sup>lt;sup>a</sup> Department of Chemistry, Lehigh University, Bethlehem, PA, 18015, USA.

<sup>†</sup> These authors contributed equally to this work.

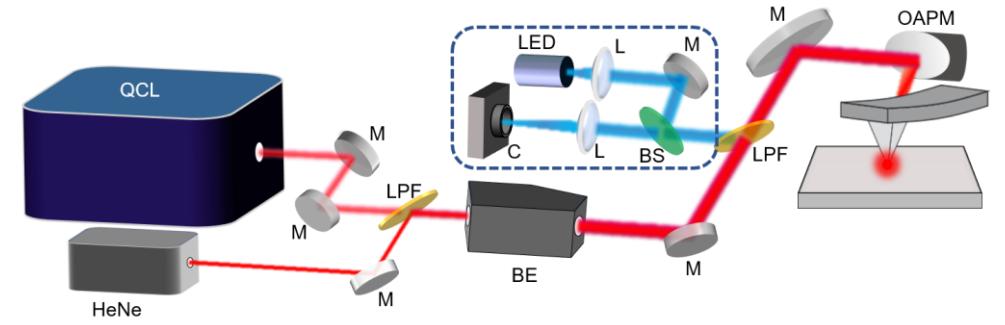


Fig. 2 The schematics of the optical path of the PFIR microscope. QCL: quantum cascade laser; M: mirror; L: lens; LPF: longwave-pass filter; BS: beam splitter; OAPM: off-axis parabolic mirror; C: camera.

of AFM-IR in recent years. In addition to IR nanoscopy in the air phase, fluid-phase AFM-IR imaging has been achieved with AFM-IRs. 11-13 The timeline of the development of modern AFM-IR techniques is summarized in Figure 1.

Peak force infrared (PFIR) microscopy is a novel AFM-IR method invented in 2017.14 PFIR microscopy is based on the pulsed force mode, 15 also popularly known as the peak force tapping (PFT) mode. The PFT mode combines advantages of contact mode and tapping mode: it has a deterministic and controlled tip-sample contact period for IR photothermal measurement; the intermittent detachment of the PFT cycle avoids the buildup of the lateral force that causes sample surface scratches. The PFT operation is also suitable for rough and sticky sample surfaces, which would otherwise cause measurement issues for the traditional contact mode AFM-IR. In addition, complementary mechanical information such as modulus and tip-sample adhesion can be readily obtained in the PFT mode through the built-in PeakForce QNM package. 16, 17 Based on PFT operation, PFIR provides IR imaging and spectroscopy capabilities through the measurement of transient cantilever oscillations triggered by the photothermal expansion of the sample induced from IR absorptions. The spatial resolution of PFIR microscopy has been demonstrated to be ~ 6 nm on a series of representative samples. 14, 18, 19 With plasmonic enhancements from metallic AFM tips, the sensitivity of PFIR has reached to zeptomolar level.<sup>20</sup>

Since the first introduction of the operation mechanism of PFIR microscopy, several technical developments and implementation variations have been made to improve performance and enable more capabilities, which are also summarized in Figure 1. These continuing developments include: a multi-pulse excitation configuration to increase signal strength;<sup>21</sup> a demonstration of the total internal reflection geometry through the evanescent field;<sup>22</sup> liquid-phase PFIR for IR nano-imaging in fluid, including water;<sup>20, 23</sup> PFIR with two independent laser sources for pump-probe and dual-color operations;<sup>24, 25</sup> an integration of PFIR with Kelvin probe force microscopy (KPFM).<sup>26</sup> In this review, we describe the construction of the original PFIR microscopy and its improved variants. Representative applications of PFIR microscopy are also included. The outlook section lays out several possible future innovations of PFIR microscopy and areas for potential applications.

# 2. Operational principle of peak force infrared microscopy

### 2.1. Peak force tapping mode

The PFT mode (e.g., Bruker's PeakForce™ Tapping) is an AFM mode that periodically modulates the tip-sample distance at a much lower frequency than the cantilever's mechanical resonance. In PFT mode, the tip momentarily indents into the sample surface, causing the cantilever to deflect vertically, which is detected by a positionsensitive quadrant photodiode. A negative feedback loop maintains the amplitude of the maximal cantilever deflection with an external setpoint. The PFT mode allows fast collections of force-distance curves to derive the mechanical properties through a model fitting, e.g., the DMT model (Derjagin, Muller, and Toropov).<sup>27</sup> A typical operation of the PFT mode simultaneously delivers sample topography, modulus, adhesion, surface deformation, and mechanical energy dissipation.<sup>28</sup> As of 2021, the PFT mode can operate up to 8 kHz, allowing for fast, non-destructive AFM imaging with deterministic tip-sample indentation force, which is suitable for delicate samples and surfaces with large height variations.

### 2.2. Optical paths, setup, and signal acquisition of PFIR

A PFIR microscope is typically built with an AFM with the PFT mode or variations equivalent to the pulsed force mode (e.g., Park's PinPoint™ mode, NT-MDT's HybriD™ mode). A representative scheme of a PFIR microscope is depicted in Figure 2. A quantum cascade laser (QCL, Daylight Solutions, MIRcat-QT) emits frequency tunable mid-IR laser pulses with durations of tens of nanoseconds. For alignment convenience, the IR beam is collinearly combined with a visible guide laser (e.g., a Helium-Neon laser of ~1 mW). The laser beam from the QCL output has a typical size of 1 to 2 mm, which is subsequently expanded by a reflective beam expander (e.g., BE04R, Thorlabs) to match the size of an off-axis parabolic mirror (N.A. 0.25). In the PFIR microscopy, a metallic AFM tip is used (e.g., HQ: NSC14/Pt, MikroMasch) to leverage the lightning rod effect. The polarization of the IR beam from QCL is parallel to the long axis of the AFM tip, enabling field enhancements. For other laser sources (e.g., OPO), the usage of a specially aligned periscope can be used to adjust the polarization of the light to the tip axis. The parabolic mirror is mounted on a three-dimensional translation stage to align the laser focus to the apex of the AFM tip. In our setup, a side-view camera system is built to check the relative positions of the tip and focus spot of the visible guide laser. The side-view camera system includes a white LED for illumination and a CMOS camera for imaging. A topview optical camera (not illustrated in Figure 2) is also used to target

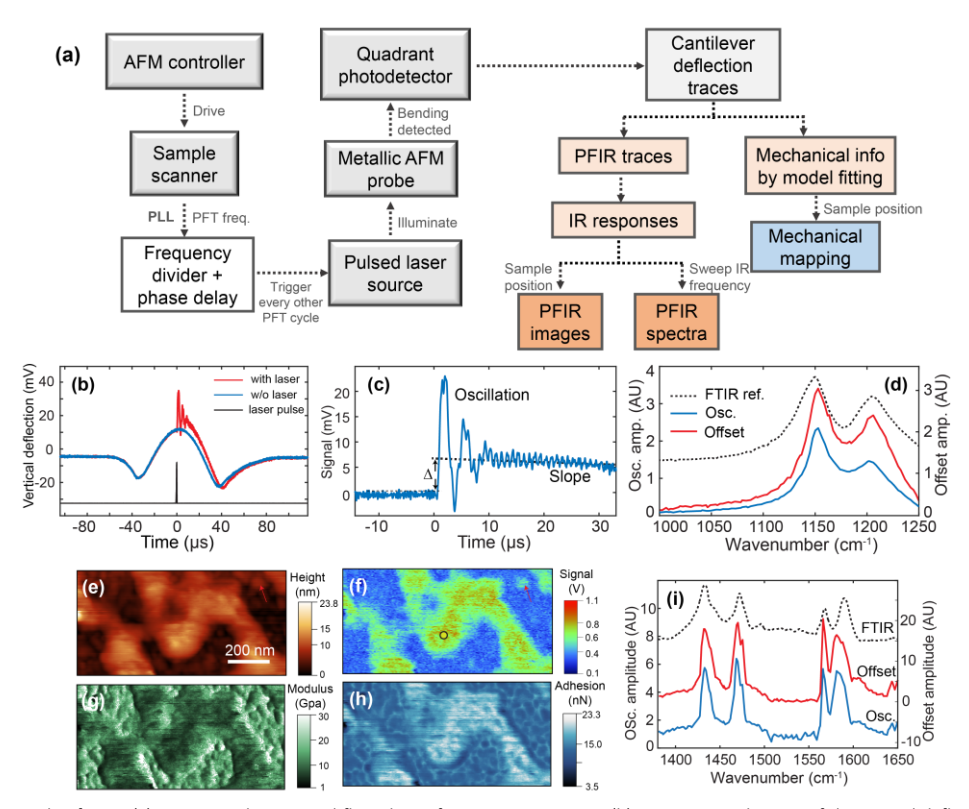


Fig. 3 The operational principle of PFIR. (a) Operation diagram and flow chart of PFIR measurements. (b) Gate-averaged traces of the vertical deflection of cantilevers with IR excitation (red curve) and without IR excitation (blue curve). The emission of laser pulses (black curve) is turned on when the tip and the sample have maximal contact. (c) A typical PFIR trace collected on a PTFE chunk. (d) PFIR spectra of PTFE plotted from the oscillation amplitude (blue curve) and baseline offset (red curve). The FTIR spectrum of bulk PTFE is included as a reference. (e-h) Topographical information, PFIR image at 1433 cm<sup>-1</sup>, modulus, and adhesion mapping of a P2VP de-wetted island on a gold substrate. (i) PFIR spectra acquired on the location marked by a black circle in (f). Both signals registered from oscillation amplitude and baseline offset are shown, together with an FTIR spectrum as a reference. (b-i) are reproduced from Ref. 14 with permission from the American Association for the Advancement of Science, copyright 2017.

the sample area of interest for the PFIR measurement. The top-view optical camera is usually a part of the commercial AFM system.

The basic working principle of PFIR microscopy is elucidated in Figure 3a. A sinusoidal voltage waveform at the PFT frequency is acquired directly from the AFM controller. It is routed to a phase-lock loop (PLL) or a lock-in amplifier (e.g., MFLi, Zurich Instrument) acting as a PLL, which generates a phase-locked transistor-transistor logic (TTL) waveform. In our initial implementation of PFIR,14 the TTL waveform was frequency-divided by two with a D-flipflop circuit and sent to trigger the QCL. In our later implementation, the frequency division was achieved by the same lock-in amplifier (MFLi, Zurich Instruments). The phase of the TTL waveform controls the timing of the emitted laser pulses. We choose the timing so that the pulse illuminates the tip-sample region when the tip and sample are in momentary contact. The exact timing of the first incident pulse is adjusted to be right after the cantilever's maximal indentation, which is usually used by the PFT mode as a process variable in the feedback loop. This implementation ensures that the PFT feedback is not affected by the photothermal response of the sample during the measurement.

In the original PFIR microscopy, the QCL emission is triggered at the exact half of the PFT frequency. Only half of the PFT cycles have laser illuminations, during which sample photothermal responses get detected by the cantilever deflection waveforms. The other half of the PFT cycles do not have laser illumination; thus, their cantilever deflection waveforms are used as a background reference. The cantilever deflection waveforms with laser illumination (Figure 3b

red curve) and without laser illumination (Figure 3b blue curve) are subtracted to reveal the pure photothermal mechanical responses of the sample and AFM tip. The subtracted cantilever deflection waveform is termed PFIR trace (Figure 3c). Three types of information can be retrieved from a typical PFIR trace: the photothermal induced oscillations, the baseline offset due to photothermal expansions, and the change of slope of the baseline. The first and second characteristics are analyzed and used to represent the magnitude of IR absorption. Here, the photothermal induced oscillation refers to the induced cantilever oscillations by the photothermal expansion of the sample, similar to that of contact mode AFM-IR.5 The amplitude of photothermal induced resonances is extracted by performing a numerical Fourier transform to the oscillations in PFIR traces. The baseline offset is calculated by fitting the baseline before and after laser excitation to obtain the difference. PFIR spectra of bulk polytetrafluoroethylene (PTFE) based on the amplitude of induced resonances and the baseline offset present high consistency with FTIR results (Figure 3d). We found that photothermal induced oscillations signals often give better signal strength than the direct measurement of baseline offset. Therefore, in our application, we typically use the photothermal induced oscillation signal as the PFIR signal for imaging and spectroscopy. If only the photothermal induced oscillation signal is used, the design of the PFIR apparatus can avoid the frequency division of the TTL laser trigger. Instead, we can use a polynomial fit to subtract the slow varying envelope from the PFT cantilever deflection to obtain the PFIR trace of photothermal induced cantilever oscillations. The

imaging capability of PFIR microscopy has been validated on poly(2-vinylpyridine) (P2VP) de-wetted islands deposited on a gold substrate, together with the modulus and adhesion information. (Figure 3e-h) The sensitivity of PFIR can be estimated from the small island marked by a red arrow in Figure 3f. We found that only approximately one thousand vibrational modes (pyridine rings) are sufficient to generate detectable PFIR signals with a signal-to-noise ratio of 3. These proof-of-principle results confirm that PFIR is a sensitive and reliable technique through the presence of local field enhancement from the metal-coated tip.

#### 2.3. Signal optimization and probe selection

The side view camera helps the alignment of the focus of the visible guide laser to the apex of the AFM tip. Afterward, we perform fine alignment based on the photothermal induced cantilever oscillations on a sample of known resonance, e.g., a spin-coated PMMA film of 50-100 nm thickness or a PTFE surface. In our customized setup, we fine-tune the position of the off-axis parabolic mirror with a three-dimensional translation stage (e.g., PT3, Thorlabs). Usually, only fine adjustments are needed to maximize the photothermal induced oscillations of the AFM cantilever.

Note that the oscillation waveforms with IR beam hitting the cantilever shaft vary drastically from those with laser hitting the tip apex and sample underneath. If the laser hits the tip and sample region, the initial photothermal expansion usually pushes the cantilever bending upward right after the laser exposure—consistent with the photothermal volume expansion of the sample. The direction of the initial cantilever deflections can be used as one necessary (but not sufficient) criterion for checking the laser alignment with respect to the AFM tip and cantilevers.

In our development, the resonant frequency of the AFM cantilever is between 100 to 300 kHz. The photothermal induced cantilever oscillations are on the order of several hundreds of kHz to MHz, usually higher than the fundamental resonance of the cantilever. The mechanical resonance of the cantilever with the tip on the sample is determined by both the geometry of the cantilever and the contact with the sample.<sup>29</sup> It typically has a resonance higher than the cantilever's free spatial oscillation. The PFIR measurement can also utilize the contact resonance of the AFM cantilever, which is

about 6.25 times the fundamental cantilever resonance. During the PFIR measurement, the photothermal induced cantilever oscillations last through the period of tip-sample contact in a PFT cycle. After the tip is detached from the sample, the mechanical resonance of the cantilever changes and can no longer support the cantilever oscillation at the same frequency. The cantilever oscillations are subsequently dampened, ensuring no leftover oscillation in the next PFT cycle, thus avoiding signal spillover to subsequent tip-sample interactions.

The AFM probe serves as an optical antenna to locally confine and enhance the IR excitation underneath the tip apex. The field enhancement is determined by the coating material and geometry of the probe. Standard commercially available AFM probes for electric force microscopy with Au and Pt/Ir coating (e.g., NSC14/15 series, Mikromasch) can readily achieve such an enhancement. In most of our applications, we prefer Pt/Ir coated tip over Au coated ones, because of higher mechanical durability of Pt coating than Au coating. Typically, commercially available metal-coated AFM probes have an apex radius of curvature of 10 – 30 nm, sufficient for the PFIR measurement. Note that in the PFIR microscopy, the contact area during the dynamic indentation can be smaller than the tip radius. In this situation, the achievable spatial resolution is better than the radius of curvature of the metal-coated AFM tips.

Complementary mechanical measurement in the PFIR microscopy requires additional consideration in choosing the spring constant of the AFM probes. In PeakForce QNM, one should select cantilevers with spring constants (k) matching the mechanical properties of investigated samples.<sup>30</sup> For example, soft cantilevers are more suitable for polymer and biological sample characterization, while stiff cantilevers are usually used for inorganic or rigid samples. If spring constants and sample's stiffness mismatch, the cantilever will either deflect without indentation (k too small) or just indent without deflecting (k too large), compromising the mechanical property mapping. A soft AFM cantilever also has a strong residual free-space oscillation after the detachment between the tip and sample in each PFT cycle, which may slightly affect the tip-sample contact regime in the next PFT cycle. A compromise of simultaneous measurement is to choose an AFM cantilever with a slightly higher spring constant for PFIR than that for PeakForce QNM.

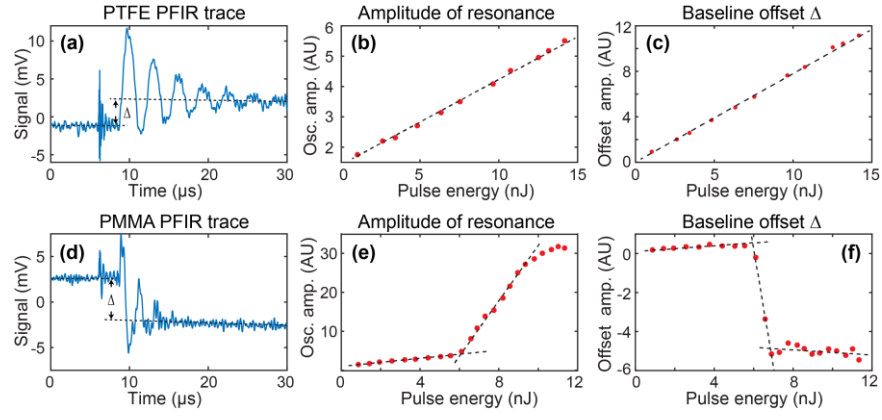


Fig. 4 Mechanical behaviors of the cantilever upon laser illumination and the power dependence of PFIR signals on a bulk PTFE sample and a PMMA film. (a)&(d) Laser-induced cantilever behaviors on PTFE and PMMA films, respectively. The laser was tuned to 1160 cm<sup>-1</sup> (symmetric CF2 stretching in PTFE) and 1725 cm<sup>-1</sup> (symmetric C=0 stretching in PMMA). Mechanical oscillations and baseline offset were observed. (b)&(e) The plot of oscillation amplitude as a function of per-pulse energy for PTFE and PMMA films at their resonance frequencies, respectively. (c)&(f) The plot of offset amplitude in PFIR traces as a function of per-pulse energy for PTFE and PMMA films at their resonance frequencies. Reproduced from Ref. 14 with permission from the American Association for the Advancement of Science, copyright 2017.

It is noteworthy that the reduction of the quality factor (Q-factor) of the AFM cantilever does not affect the signal quality because the measurement of photothermal induced cantilever oscillations only lasts for several tens of microseconds. The Q-factor of common probes is sufficient so long as the cantilever oscillation can last till the detachment between the tip and the sample. In fact, AFM probes with a low Q-factor may even be preferable in practice to minimize free-space oscillations after tip-sample detachment that may cause residual background into the PFIR signal of the next PFT cycle.

### 2.4. Power dependence of PFIR signals

With the field enhancement from the AFM tip, intense IR illumination on the tip-sample in contact could cause sample surface damage on soft matters if too much heat was generated. On the other hand, the PFIR signal scales with the input IR pulse. Therefore, a meaningful question for the operation of the PFIR microscopy would be what the maximal IR energy per pulse is that one can use for the measurement without compromising the sample integrity. We have examined the relationship between pulse energy and the PFIR signals on PMMA and PTFE polymer surfaces. The PMMA film in this experiment was prepared by spin-coating PMMA from the toluene solution onto a gold substrate; the PTFE sample was cut from a bulk of PTFE material. In our experiment, an AFM tip was continuously tapping at a fixed location on the sample surface under the PFT feedback. The PFIR signals were recorded while IR pulse energy gradually ramped up. Two PFIR signal channels were registered in parallel: (a) from the photothermal induced cantilever oscillations; (b) from the baseline offset in PFIR traces before and after IR pulses.

If the photothermal effect is strong enough, amorphous polymer samples can undergo glass transitions from a glassy state to a rubbery state. For crystalline polymer, the sample can undergo a phase transition from solid to liquid. In both cases, the sample surfaces are vulnerable to deformation. Figure 4a is a typical PFIR trace collected on the PTFE sample after subtraction of the cantilever deflection waveforms with and without IR illumination. A positive baseline offset is observed due to the volume expansion, as well as photothermal induced cantilever oscillations from the rapid

expansion of the sample right after the IR illumination. Figure 4b-c shows the relationship between PFIR signals versus IR pulse energy of the PTFE sample. Clear linear dependence between the signal and the laser power is observed in the oscillation amplitude channel and the baseline offset channel.

However, the PFIR signal dependence on the PMMA sample did not follow a simple linear behavior. The measurement results are displayed in Figures 4d-f. Figure 4d shows a PFIR trace with a negative baseline offset upon IR pulse illumination at a high energy level, showing an apparent "reduction" of the volume, indicating possible glass transition.31 This behavior differs from the positive baseline offset of PTFE Figure 4a. In Figure 4e, the amplitude of the photothermal induced cantilever resonance oscillations shows two linear regions, followed by curvature at the high energy level. In Figure 4f, the baseline offset initially exhibits a positive linear trend versus the pulse energy, indicating volume expansion. After a threshold value, a discontinuity of the power dependence is observed, and the baseline offset becomes negative. These observations indicate that within the low power regime, PMMA behaves similarly to the bulk PTFE sample with linear IR energy dependence. After the local temperature increase from the photothermal effect surpasses the glass transition temperature (Tg), the PMMA sample surface becomes rubbery, with reduced mechanical modulus, and is vulnerable to surface deformation. Above T<sub>g</sub>, the PFIR signal versus pulse energy loses the linear trend in both the oscillation amplitude channel and the baseline offset channel. The reason of different behaviors between PMMA and PTFE is likely due to stronger field intensity underneath the AFM tip in the PMMA measurement: gold substrate was used to increase field enhancement in the PMMA measurement; the far-field optical density of PMMA measurement was higher due to a smaller laser focus of a shorter wavelength light of 1725 cm<sup>-1</sup> compared with 1160 cm<sup>-1</sup> in the case of PTFE. Moreover, the per photon energy for carbonyl resonance is higher than that of the C-F stretching of PTFE. The photothermal responses scale with the total energy absorption, which is the number of absorbed photons multiplied by the energy per photon.

The energy dependence from PTFE and PMMA samples provides an insight into how to set up a suitable PFIR microscope that

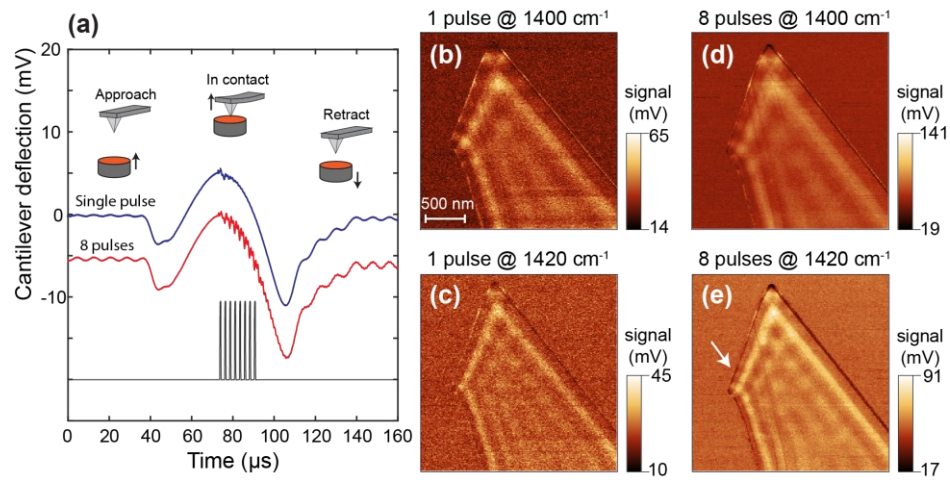


Fig. 5 Signal enhancement from multi-pulse PFIR scheme. (a) Cantilever deflection traces in PFIR with one laser pulse (blue curve) and eight laser pulses (red curve). The timing of the emitted laser pulse train is shown as the black curve. Insets illustrate the sample movement during one peak force tapping cycle. (b-e) PFIR images obtained on hexagonal BN micro-flakes at 1400 cm<sup>-1</sup> and 1420 cm<sup>-1</sup> with 1-pulse and 8-pulse excitation schemes. Reproduced from Ref. 21 with permission from John Wiley and Sons, copyright 2019.

produces a strong signal. The IR pulse energy should be kept within the linear regime and set below any possible glass transition or phase transition. Within the linear regime, the PFIR signal is practically proportional to the IR absorbance of the sample—a condition that all AFM-IR techniques are aimed for.

An advantage of the PFIR microscopy, compared with the resonance-enhanced AFM-IR, PiFM or tapping mode AFM-IR, is that the repetition rate of the IR light source is low and on the order of a few kHz instead of hundreds of kHz or MHz. Therefore, the accumulation of heat from the PFIR measurement is minor and non-destructive to thermally unstable samples, such as perovskite photovoltaic materials.<sup>14</sup>

### 2.5. Multi-pulse modality of PFIR to push the limit of sensitivity

The PFIR signal originates from photothermal expansion. The photothermal responses are usually weak on samples with relatively small thermal expansion coefficients, resulting in low PFIR signals. For example, inorganic materials have lower thermal expansion coefficients than soft matters.<sup>32, 33</sup> To improve the signal quality of the PFIR microscopy on materials with low thermal expansion coefficients, we have developed a multi-pulse infrared excitation modality, similar to the improvement of REINS over the regular contact mode PTIR. In the original version of the PFIR microscopy, only one infrared pulse was utilized per PFT cycle. <sup>21</sup> In the multi-pulse excitation scheme, a train of laser pulses are emitted upon the trigger in one PFT cycle. The temporal interval between pulses is set to match the cantilever oscillation period while the tip being in contact with the sample.<sup>34</sup> If a high quality factor (Q-factor) cantilever is used, the cantilever oscillations from the photothermal response of the sample add up in phase, leading to enhanced PFIR signals. Alternatively, the temporal spacing of the laser pulses can be chosen to avoid the cantilever resonance. In this case, the signal crosstalk between the mechanical properties and the IR signals is reduced. Figure 5a shows the comparison of cantilever deflection traces with one-pulse and eight-pulse excitation, as well as the timing of IR pulses. The improvement of imaging quality and enhancement of signals are demonstrated in Figure 5b-e to image the interference patterns of phonon polaritons (PhPs) in h-BN. One can observe that with 8-pulse excitation, PFIR signals are significantly improved with a higher signal-to-noise ratio of 37  $\pm$  1.5 compared with 13  $\pm$  1.2 in the one-pulse case. In Figure 5e, small patterns, such as weak polariton interference fringes (marked by a white arrow), can be identified, which is not visible in Figure 5c. In imaging PhPs, the multi-pulse PFIR is capable of serving as an alternative to s-SNOM with photothermal signal readouts.

### 2.6. Total Internal Reflection PFIR Microscopy

In addition to the side illumination geometry described in previous sections for the original PFIR microscopy, another feasible optical delivery configuration is through the total internal reflection. The total internal reflection (TIR) usually involves an internal reflection element (e.g., prism) that are made of IR-transparent materials with high refractive indices (e.g., ZnSe, Si, Ge, and diamond).<sup>35</sup> When the IR beam propagates from the high refractive index region to a low refractive index region (e.g., air), and the incident angle exceeds the critical angle of the high /low refractive indices interface, total

internal reflection occurs. While IR does not propagate into the low refractive index region, a confined and decaying evanescent field is established at the interface to the range of a fraction of the wavelength. Vibrational resonances of molecules and materials can be excited by the evanescent field established by the TIR of IR light.

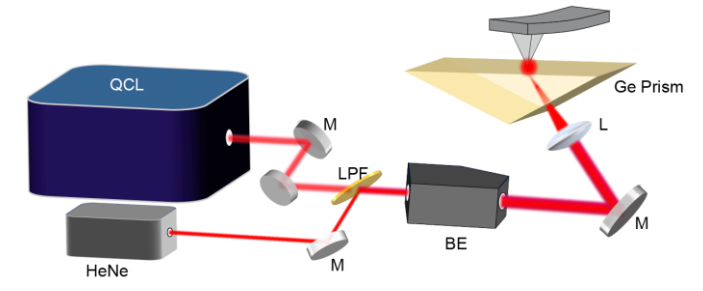


Fig. 6 Experimental setup up of TIR-FTIR. The mid-IR radiation (with 40 - 1000 ns pulse duration) from QCL (MIRcat-QT, DRS Daylight Photonics) is combined with a guide HeNe laser at a longwave pass filter (LPF). The combined beam is further expanded by a beam expander and focused on the prism/air interface by an IR lens.

An AFM tip placed on top of the total internal reflection element and within the range of the evanescent field can detect the photothermal response of the sample. The initial contact mode AFM-IR experiment was accomplished with the TIR geometry in 2005.<sup>7</sup> The signal detection principle of the PFIR microscopy is compatible with the TIR configuration, which leads to the development of the total internal reflection peak force infrared (TIR-PFIR) microscopy.

A representative optical configuration for TIR-PFIR is illustrated in Figure 6. TIR-PFIR microscopy shares the same signal detection and processing mechanism as the regular PFIR microscopy, as most optical elements used for laser steering and expansion are similar. For the generation of evanescent field from TIR, an IR-transparent prism (e.g., Ge prism) is adopted as the AFM substrate. The pulsed (40 – 1000 ns) mid-IR radiation from QCL is brought from the bottom and focused onto the prism/air interface, with an incident angle matching the critical angle of the interface to ensure maximal field enhancement.<sup>20</sup> Instead of a parabolic mirror, an IR lens made of Ge (Edmund Optics, f =2.5 cm) is used to focus due to the ease of achieving the critical angle in this bottom-up configuration. In TIR-PFIR, the requirements for tight focusing are not as stringent as in the case of regular PFIR because the additional field enhancements brought by the evanescent field compensate for the photon fluence reduction caused by loose focusing. The polarization of the IR light is chosen to be p polarized with respect to the incident plane for strong field enhancement. The evanescent field is further enhanced by the metal-coated AFM tip, exciting the sample volume underneath the tip and causing photothermal expansions at the moment of tipsample dynamic contact in the PFT cycle. The multi-pulse PFIR method can be integrated into TIR-PFIR, where a train of mid-IR pulses with the repetition rate matched to one of the cantilever's oscillation frequencies is turned on in every PFT cycle to increase the mechanical response of the cantilever to photothermal expansion. In principle, any PFT-enabled AFM platform with proper modifications on the sample stage could be used to build up TIR-PFIR, so long as the total internal reflection prism can be mounted. In our proof-ofprinciple TIR-PFIR setup, Bruker Bioscope Catalyst were used, because it allows optical access from the bottom that was reserved for an inverted optical microscope. AFM of similar designs, such the more recent Bioscope Resolve or JPK's Nanowizard V, should be

suitable in building a TIR-PFIR setup. The alignment procedure and proof-of-principle demonstration is described in the Supplementary Material for the sake of conciseness.

Although the usage of the TIR prism is often associated with additional cost, the TIR-PFIR microscopy has several advantages in certain applications compared to the regular side-illumination PFIR microscopy. One of the advantages of TIR-PFIR is the additional enhancement brought by the evanescent field, which leads to reduced background and allows for the use of a loose focus. Given the general AFM tip height of  $10 - 20 \mu m$ , the majority of decaying evanescent fields will contribute only to the tip-enhancement region underneath the AFM tip, rather than illuminate the shaft of the cantilever. In contrast, the side-illumination used in regular PFIR inevitably shines on the AFM cantilever and causes unwanted nonsample specific cantilever oscillations. From an application perspective, the TIR configuration of PFIR opens the possibility for in situ in operando nanospectroscopy at the solid/air interface that requires changing the type and pressure of the reaction gas ondemand. For the side-illumination scheme of PFIR involving tight focus of the IR beam to the sample from the side, a large gas chamber would be needed to enclose the optical elements. On the other hand, the TIR geometry permits the usage of a smaller chamber, so long as it can enclose the AFM cantilever and seal on the TIR prism. Another advantage of the TIR configuration is that it opens a route toward liquid-phase PFIR microscopy, which will be discussed next.

#### 2.7. Liquid phase PFIR microscopy

Two major challenges of IR microscopy are the limited spatial resolution and the incompatibility with the fluid phase or aqueous phase applications due to large background absorptions. The photothermal detection of the AFM-IR bypasses Abbe's diffraction

limit, improving the spatial resolution to the nanoscale. In addition, the mechanical detection of local photothermal expansion also permits the reduction of the artifacts caused by the background absorptions of solvents. The first in-liquid imaging of fungi cells was reported in 2008 with ~100 nm resolution. Recent years have witnessed significant advancements in the development of AFM-IR microscopy in liquids. REINS, developed by Belkin and coworkers, achieves 25-nm spatial resolution on polymer samples in heavy water. The similar resonance enhanced AFM-IR method was later applied in detecting secondary structures of polypeptides in water by Centrone and colleagues. 13

Our group has developed the PFIR microscopy into the fluid phase through the TIR configuration and demonstrated it on several representative samples.<sup>22</sup> The liquid phase PFIR microscopy shares the same apparatus as the TIR-PFIR microscope. A fluid chamber enclosing the AFM tip and sealing the liquid on the TIR prism is added onto the sample stage. The beam incident angle is adjusted to match the critical angle incidence at the prism/liquid interface. Figure 7a depicts the setup of the liquid phase PFIR microscope.

# 2.7.1. Challenges of fluid operation in liquid-phase PFIR microscopy

Typical IR microscopy requires the delivery of the IR radiation to the sample and the collection of the IR radiation after attenuation caused by the light-matter interaction. The strong IR absorption by water means the reduction of the signal in both beam delivery and collection for optically detected IR microscopy, such as the recently developed aqueous phase s-SNOM.<sup>36-38</sup> In comparison, the mechanical detection of the photothermal response only suffers from the IR beam delivery loss. By using the TIR configuration, the IR delivery loss is greatly alleviated. The IR evanescent field only

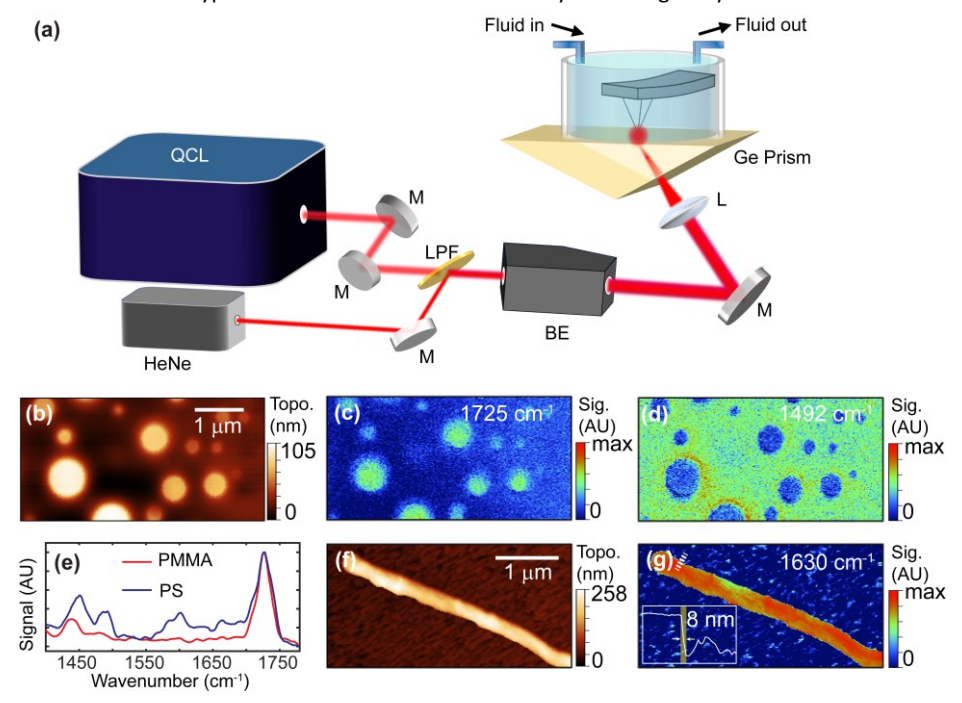


Fig. 7 Experimental apparatus and demonstration of liquid-phase PFIR. (a) Experimental setup of liquid-phase PFIR. A fluid chamber is installed on top of the prism. The fluid chamber is equipped with a liquid inlet and outlet, allowing for constantly changing the liquid environment. (b) Topography of PS:PMMA polymer blends in heavy water. (c-d) Liquid-phase PFIR images at 1725 cm<sup>-1</sup> (PMMA) and 1492 cm<sup>-1</sup> (PS), respectively. (e) Point spectra collected from PMMA (red) and PS (blue) domains. (f) Topography of a BSA protein fibril in water. (g) Liquid-phase PFIR image at 1630 cm<sup>-1</sup>, corresponding to amide I absorption of proteins. Inset shows signal profile extracted from the white dashed curve in (g), where the spatial resolution of 8 nm is obtained. (b-g) are adapted from Ref. 20 with permission from American Chemical Society, copyright 2021.

penetrates several microns into the fluid and is subject to attenuation. The photothermal expansion signals from the sample are transduced into the cantilever deflections and are locally read out by the AFM tip, bypassing the signal loss through the optical detection.

Another challenge arises from the strong damping of the cantilever oscillation by the hydraulic drag of the liquid. A metric to consider is the Q-factor of the cantilever, which describes the ratio between the total energy stored in cantilever oscillation versus dissipated energy per oscillation cycle. The Q-factor is reduced by approximately two orders of magnitude in water than in air.<sup>39</sup> The photothermal induced cantilever oscillation for the sample expansion is rapidly damped if the cantilever is surrounded by water. On the other hand, the contact mode and tapping mode AFM-IR reads out signals through lock-in detection. The higher the Q-factor is, the stronger the oscillation amplitude for the AFM-IR. Consequently, the AFM-IR operation in fluid suffers strongly from the hydraulic drag, leading to a reduction of signal quality.

In contrast, PFIR microscopy suffers less from the hydraulic drag of the cantilever oscillation than other AFM-IR modality, because the signal read-out of PFIR microscopy does not require the oscillation from the cantilever to last longer than the tip-sample contact period. The read-out window is only several tens of microseconds, corresponding to a few cantilever oscillation cycles. A single-digit Qfactor is sufficient for PFIR signal read-out. Moreover, the liquidphase PFIR can directly register the photothermal expansion of samples from the baseline offset channel, manifested as a small transient jump or drop in the cantilever deflection waveform after IR pulse illumination. This direct measurement of the expansion signal does not involve the measurement of cantilever oscillation and is independent of the Q-factor. In our proof-of-principle liquid-phase PFIR apparatus, we implemented a multi-pulse PFIR scheme to generate multiple photothermal expansion events per PFT cycle to compensate for the weak signal. Also, because the photothermal expansion of the sample in the fluid phase is typically weaker than that in the air phase due to much faster thermal dissipation by the fluid, the background subtraction scheme of the original PFIR microscopy that illuminates the sample for every other PFT cycle can be modified. Instead, a simple polynomial fitting is sufficient to remove the slow varying curvature from the tip indentation to the sample. Consequently, in the liquid phase PFIR, IR pulses are synchronized with every PFT cycle. The cantilever deflection trace is processed in real-time by fitting the slow varying curvatures, followed by subtraction. The result is that the data acquisition speed is doubled in liquid-phase PFIR.

# 2.7.2. Alignment of the liquid-phase PFIR apparatus

In general, the alignment of liquid-phase PFIR is almost the same as the alignment in TIR-PFIR except for the difference between water and air. Compared to air, the mechanical resonant frequency of the cantilever decreases in water, i.e.,  $\Omega_{\text{water}} < \Omega_{\text{air}}$ . Besides, the Q-factor of the cantilever drops significantly in water. As a result, alignment in water is more complex than that in the air because the photoacoustic (PA) signals detected by the cantilever (see Supplementary Materials) are much smaller. Therefore, the whole liquid-phase PFIR setup is first aligned in the air with standard samples, and then the standard sample can be replaced by the sample of interest in liquids while keeping the same alignment as

much as possible. The optical path of the IR beam delivery for TIR-PFIR and liquid-phase PFIR should be the same. If the sample of interest does not hold strong IR absorptions and PA signals, the fine-tuning of the alignment can be achieved by tuning the IR pulses to water absorption (e.g., 1630 cm<sup>-1</sup>) or other solvent absorptions and maximizing the PA signal.

Our proof-of-principle liquid-phase apparatus is equipped with a silicone fluid cell that is compatible with common solvents. The fluid cell also permits fluid flow to maintain or change the composition of liquid environments. Based on the IR absorption of the used solvent, additional experimental data are needed to interpret nano-IR maps and assign point spectra unambiguously. For example, to confirm the existence of IR bands (e.g., amide groups) within the IR absorption of water, heavy water can be used as a replacement to water with a transparent window between 1500 - 1700 cm $^{\text{-}1}$ . A background spectrum measured on the bare Ge substrate should be collected if the interested IR absorption overlaps with the solvent absorption.

The choice of AFM probes is also important in liquid-phase PFIR microscopy. Selected AFM probes must support strong field enhancements and be stable in liquids. For this reason, Au-coated probes are mostly used in liquid-phase PFIR microscopy. Cantilevers with AI coatings tend to deteriorate in water and thus should be avoided.

#### 2.7.3. Depth of the IR penetration in water

The penetration depth of TIR is proportional to the wavelength. A longer wavelength of IR leads to longer penetration depths in the water. For instance, the calculated penetration depth for 6.25  $\mu m$  light at the Ge/water interface is 3.3  $\mu m$  with an incident angle of 20°. As the incident angle gets closer to the critical angle, the penetration depth increases rapidly. Such long penetration depths render liquid-phase PFIR suitable for imaging not only solid/liquid interfaces and thin films but also samples up to a few microns, such as biological cells.

Although liquid-phase PFIR microscopy benefits from longer IR penetration depths, in practice, the light penetration in liquid-phase PFIR with thick samples also depends on many other factors, such as sample structure and bulk absorption. For example, for highly uneven samples, the light delivery is heterogeneous and may distort the true IR characteristics of the sample surface. Moreover, a thick absorbing layer can further attenuate the IR power, leading to a higher background, inefficient tip-enhancement, decreased sensitivity, and reduced spatial resolution. Therefore, cautions are needed when applying liquid-phase PFIR microscopy to the measurement of thick samples.

### 2.7.4. Proof-of-principle demonstration of liquid-phase PFIR

The nano-IR imaging capability of liquid-phase PFIR has been demonstrated on phase-separated polymer blend film. Figures 7b-d show liquid-phase PFIR imaging results on a 250-nm thick PS:PMMA blend film. Similar to TIR-PFIR, liquid-phase PFIR microscopy clearly distinguishes PS and PMMA nanodomains based on their IR absorptions in liquids. Spectra obtained from each domain (Figure 7e) mainly exhibit IR signatures of PS and PMMA, respectively, indicating adequate chemical sensitivity of liquid-phase PFIR microscopy. Because polymer blends are phase-separated only on

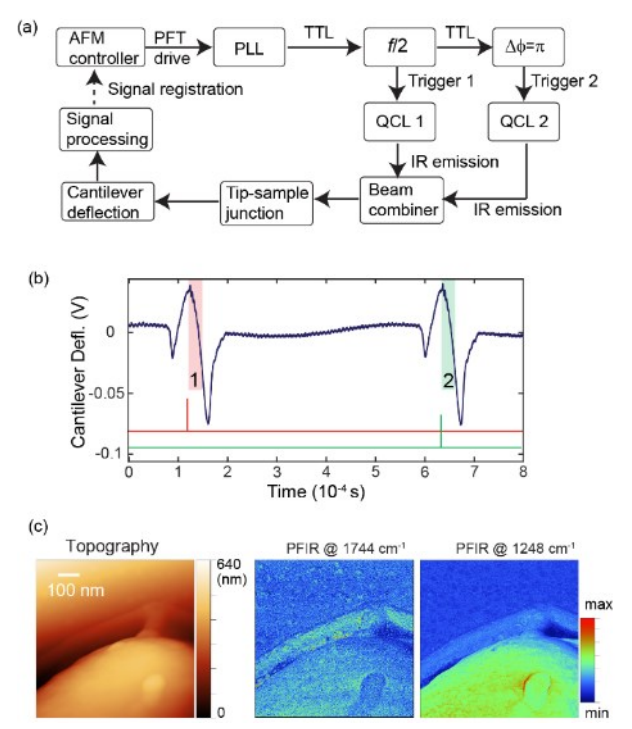


**Fig. 8** Dual-color PFIR microscopy. (a) Signal generation flow chart of dual-color PFIR microscopy. (b) Schematic illustration of the timing of two IR pulses during a consecutive PFT cycle. (c) Demonstration of dual-color PFIR microscopy on an edge of E Coli cell with outer cell membrane. (b) and (c) are adapted from Ref. 25 with permission from American Chemical Society, copyright 2022.

the surface but mixed in bulk, the strong carbonyl peak at 1725 cm<sup>-1</sup> is visible in both spectra due to the bulk absorption of PMMA.

Proteins are large biomolecules that play central roles in building and regulating complex biological systems. Multiple characteristic IR amide bands are present in protein structures, allowing them to be identifiable through IR spectro-microscopy. Figures 7f-g show liquid-phase PFIR images of a protein fibril formed by bovine serum albumin (BSA) in water. The BSA fibril is roughly 150-nm high and 350-nm wide, and its strong amide I absorption at 1630 cm<sup>-1</sup> clearly distinguished itself from the non-absorbing substrate. The spatial resolution of liquid-phase PFIR microscopy is estimated from the edge of the BSA fibril (Figure 7g, inset), which is close to 10 nm and consistent with TIR-PFIR.

#### 2.8 Dual-color PFIR microscopy

One application of PFIR microscopy, and nano-IR microscopy in general, is to determine the relative spatial distributions between two different chemical components of heterogeneous materials and structures. It is typically done through sequential AFM scans, i.e., acquisition of one PFIR image frame with the QCL tuned to one IR frequency for the first chemical component and then the acquisition of the second PFIR image frame with the QCL tuned to the other IR frequency for the second chemical component. However, possible position drift and distortion exist between two sequential AFM frames, especially for AFMs with an open-loop piezo scanner, such as the Multimode product line from Bruker.

To bypass the limitation of frame drift and distortion among sequential AFM scans, the dual-color PFIR microscopy was developed by our group in 2021.<sup>25</sup> Figure 8a illustrates the signal generation flow chart of dual-color PFIR microscopy. In this technique, two QCLs

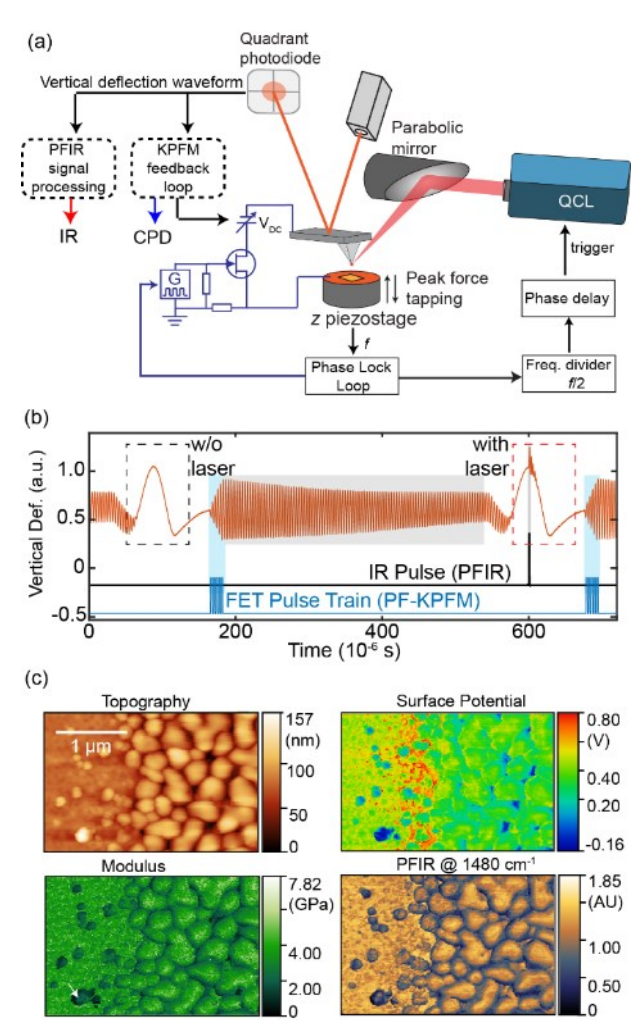


Fig. 9 Combining IR and surface potential measurements in PFIR-KPFM. (a) Experimental setup and schematics of PFIR-KPFM. (b) Trigger timings and signals of PFIR-KPFM. (c) Correlative surface potential, modulus, and IR imaging on the perovskite MAPbBr<sub>3</sub> crystal surface. Reproduced from Ref. 26 with permission from John Wiley and Sons, copyright 2020.

are used to provide two IR radiations of different frequencies. The optical paths of the two IR beams are combined with a 50:50 IR beam splitter and guided to the tip-sample junction of the AFM microscope. The timing of the emission of the IR pulses from each QCL is synchronized with every other PFT cycle through the combination usage of PLL and time/phase delay. The IR lasers illuminate the sample when the tip and sample is in dynamic contact during a PFT cycle. In our implementation, we use the MFLi-MD lockin amplifier (Zurich Instrument) to generate the phase locked TTL trigger waveforms at the exact half of the PFT frequency to trigger the laser emission of the first QCL. A replica of the TTL waveform with  $\pi$  phase delay is generated by the same lock-in amplifier and used to trigger the IR emission of the second QCL. The data acquisition card and embedded controller continuously acquire and process the vertical deflection signal from the AFM. One of the two TTL trigger waveforms is also simultaneously acquired with the cantilever vertical deflection signal, and used as a criterion by the customized software to identify and sort the photothermal signals according to its IR source frequency. The two sorted photothermal PFIR signals (Figure 8b) are simultaneously routed to the AFM controller and to

be registered with the lateral positions of the AFM tip for dual-color PFIR images at two IR frequencies (Figure 8c).

The usage of two QCLs also opens the door for the frequency-domain pump-probe PFIR microscopy. In the frequency-domain pump-probe PFIR microscopy, the two independently tunable IR pulses from the two QCLs arrive during the tip-sample contact and jointly generate photothermal responses. Depending on the molecular structures of the sample, simultaneous illumination from the two IR frequencies may open sequential spectroscopic pathways when single IR frequency alone cannot, such as excited state absorption for vibrational oscillators with anharmonicities, or ground state depletion. The difference on photothermal responses between temporal overlap and offset of two frequency tunable QCL pulses are obtained and used to represent the contribution from the joint spectroscopic pathways. The details of a demonstration of the frequency domain pump-probe PFIR microscopy is describe in our recent paper.<sup>24</sup>

# 2.9 Integration of PFIR microscopy with surface potential measurement for high-throughput multimodal imaging

AFM is often dubbed as the "Swiss army knife" of surface nanoscale analysis in that it delivers a convenient platform to achieve multimodal characterizations. The PFIR microscopy enables simultaneous chemical composition and mechanical property collections in one AFM scan. In 2020, our research group has further integrated the PFIR microscopy with surface potential measurement in one AFM scan, which result in the method of peak force infrared-Kelvin probe force microscopy (PFIR-KPFM).<sup>26</sup>

While traditional Kelvin probe force microscopy (KPFM) is typically performed with the tapping mode AFM, our research group has developed a variation of KPFM that operates in the pulsed force mode, which is equivalent to the PFT mode. 40 In this pulsed force KPFM, the surface potential measurement is performed during the PFT cycle when the tip and sample are just momentarily detached. A field effect transistor (FET) is used to periodically switch the electric connectivity between the AFM tip and the sample surface. When the metal-coated tip and the sample surface is electrically connected, the

Fermi-level alignment causes electrons to migrate according to their contact potential difference (CPD). As a result, Coulombic force emerges as a result of appearance of charges between the AFM tip and sample. The period between the FET switching is chosen to match that of the free space cantilever oscillation period, so the mechanical effects from the Coulombic force are amplified. A negative feedback loop is then used to regulate the magnitude of the Coulombic force with a set point as the KPFM feedback. As the procedure described in our pulsed force KPFM literature, 40 the CPD is obtained as the AFM tip scanning over the sample.

In the joint operation of the PFIR-KPFM, both the tip-sample contact regime and the tip-sample detachment regime of the peak force tapping mode are utilized. Figure 9a displays the schematic of the PFIR-KPFM setup. A pulsed force KPFM circuit between the sample and tip is built into a standard PFIR microscopy apparatus. During PFIR-KPFM operation, the IR laser emissions are synchronized to the tip-sample contact regime to generate photothermal expansions; the connectivity switching through the FET to generate Coulombic force right after the tip-sample detachment for KPFM feedbacks. Representative waveforms of cantilever deflection signal, laser pulse emission, and FET switching timing are displayed in Figure 9b. The photothermal detection channel of the PFIR and the surface potential detection channel of the pulsed force KPFM are carried out in parallel within two different regimes of tip-sample interactions. Consequently, there is no cross-talk between the KPFM measurement and the PFIR measurement. These two distinctive signal channels are registered simultaneously, together with the topography and mechanical properties from peak force tapping mode operation through the standard PeakForce QNM package from Bruker's AFM. Figure 9c displays a simultaneous measurement of topography, surface potential, modulus, and PFIR images on a degraded surface of MAPbBr<sub>3</sub> perovskite crystal.<sup>26</sup> The measurement was obtained in one AFM scan frame. This measurement reveals accumulation of charges in the MAPbBr<sub>3</sub> region near PbBr<sub>2</sub>, due to positions of Fermi Levels.

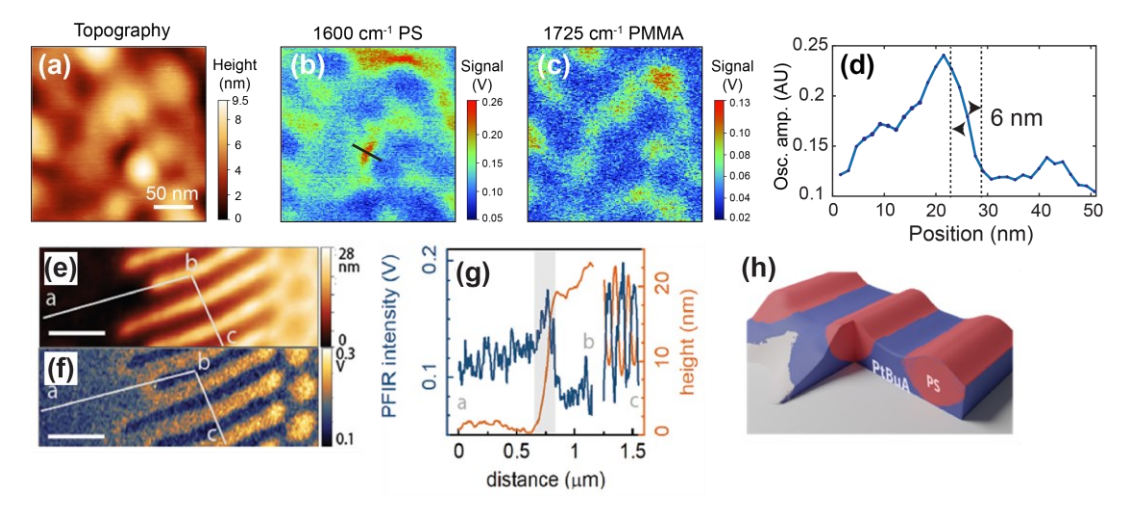


Fig. 10 Applications of PFIR microscopy in revealing chemical and mechanical information of self-assembled diblock copolymer patterns. (a-c) Topography and PFIR images at 1600 cm<sup>-1</sup> and 1725 cm<sup>-1</sup> on a PS-b-PMMA phase-separated pattern. The infrared frequency of 1600 cm<sup>-1</sup> corresponds to the stretching mode of C-C in aromatic rings in polystyrene, while 1725 cm<sup>-1</sup> is on the resonance of symmetric stretching of C=O bonds in PMMA. (d) Spatial resolution is estimated from a cross-section line profile marked in (b). (e-f) Topography and PFIR image at 1728 cm<sup>-1</sup> (C=O stretching), representing the distribution of PtBuA. Scale bars are 500 nm. (g) Cross-section line profiles along the marked lines ab and bc in (e-f). (h) A schematic of the interfaces of PS and PtBuA domains showing how the two components are structured. (a-d) are adapted from Ref.14 with permission from the American Association for the Advancement of Science, copyright 2017. (e-h) are adapted from Ref. 47 with permission from American Chemical Society, copyright 2021.

# 3. Applications of PFIR microscopy in the air phase

The PFIR microscopy has been demonstrated on a wide range of chemical and biological samples since its invention in 2017. For example, the PFIR microscopy has been utilized to identify chemical components of nano-phase separation of block copolymers, <sup>14</sup> field-collected secondary organic aerosols, <sup>41</sup> phonon polaritons supported by boron nitride, <sup>34</sup> wood fibers, <sup>42</sup>, <sup>43</sup> protein aggregates and biological cells, <sup>19</sup> surface chemical distributions of perovskite and organic photovoltaic films. <sup>19</sup>, <sup>44</sup>, <sup>45</sup> PFIR with polarized laser beam has been utilized to investigate surface chemistry on 2D metal-organic layers (MOLs). <sup>46</sup> In the following subsections, we will describe several representative applications of the PFIR microscopy in the air phase.

# 3.1. Chemical and mechanical maps of phase-separation patterns of block copolymers

Segments of the block copolymers tend to segregate and form nanostructures or nanophase separations when placed under confined spaces. The final morphology of phase separation is impacted by temperature, the molar ratio of different polymer blocks, the choice of solvents, and other factors. The PFIR microscopy is a feasible technique for nanoscale chemical and mechanical mapping on the self-assembled polymer patterns. Figures 10a-c present the morphology and PFIR images of the phase-separated pattern of polystyrene-b-poly(methyl methacrylate) (PS-b-PMMA) with the thickness of the film approximately 30 nm. The PFIR images were registered using the amplitude of photothermal induced cantilever oscillations. The PFIR images at 1600 cm<sup>-1</sup> (stretching mode of PS aromatic rings) and 1725 cm<sup>-1</sup> (stretching mode PMMA C=O bonds) show complementary spatial features that correspond to the nanophase separation of PS and PMMA domains. A spatial resolution of 6 nm has been achieved, estimated from a cross-section profile along with the marked position in Figure 10d. Dr. Gilbert Walker and colleagues demonstrated the application of PFIR in revealing the structural organization of polystyrene-b-poly(tert-butyl acrylate) (PS-b-PtBuA) phase-separations through combining mechanical information and sub-surface chemical compositions (Figure 10e-h).<sup>47</sup> By uncovering IR peak shifts, they observed polymer chains under various tensile strains at different film boundaries. From the results mentioned above on block copolymers, one can

conclude that PFIR microscopy is a powerful tool with high spatial resolution and high sensitivity for simultaneous mechanical and chemical-specific imaging. These capabilities are much needed to obtain an in-depth understanding of the mechanism of the polymer self-assembly process.

# 3.2. Compositional analysis of fine and ultrafine indoor aerosol particles

Particulate matters, also known as aerosols, are nanoscopic or microscopic solid particles or liquid droplets suspended in the air.  $^{48}$  Indoor aerosols can negatively affect human health and have attracted growing public attention as people have spent more time indoors during the pandemic of COVID-19.  $^{49,50}$  Although appropriate filters can remove most of the large-sized aerosols, fine and ultrafine aerosol particles of diameters less than 2.5  $\mu m$  and 0.1  $\mu m$  respectively still post challenges to human health due to their long diffusing time, high airborne mobility, and large penetration depth in respiratory systems. The source of indoor aerosols can be natural or anthropogenic, leading to a significant structural and compositional heterogeneity of inter- and intra-particles. Characterization techniques that provide access to individual particles are required to reveal varying chemical and organizational information of indoor aerosols.

PFIR microscopy has recently been successfully applied to identify intraparticle chemical species and their correlative mechanical properties of fine and ultrafine indoor aerosols.51 The field-collected aerosols were from a local grocery store, a residential house, and office space in the PI's lab with a three-stage particle sampler (MPS-3, California Measurements). Figure 11 demonstrates two aerosol clusters with their topography, modulus, adhesion, and PFIR images at 1660 cm<sup>-1</sup> (amide I bond in proteins) and 1725 cm<sup>-1</sup> (symmetric stretching of C=O bonds). The capability of collecting intraparticle point spectra enables a detailed look at compositional heterogeneity. The grainy aerosol particle in Figure 11a features a biological origin in view of pronounced IR absorption peaks of amide bonds, while the aerosol cluster in Figure 11b is more likely attributed to triglyceride-adsorbed soot agglomerates given the strong signal of carbonyl entities. Both < 500 nm fine aerosols and < 100 nm ultrafine aerosols (marked by a white arrow in Figure 11b) are revealed in the shown data.

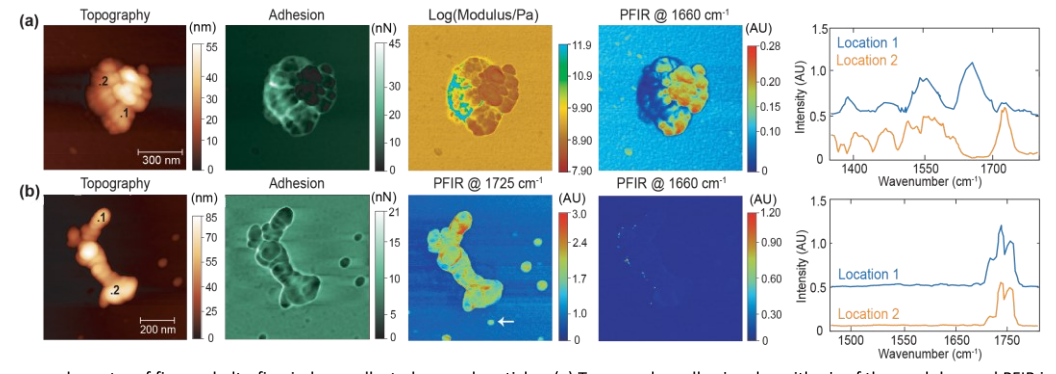
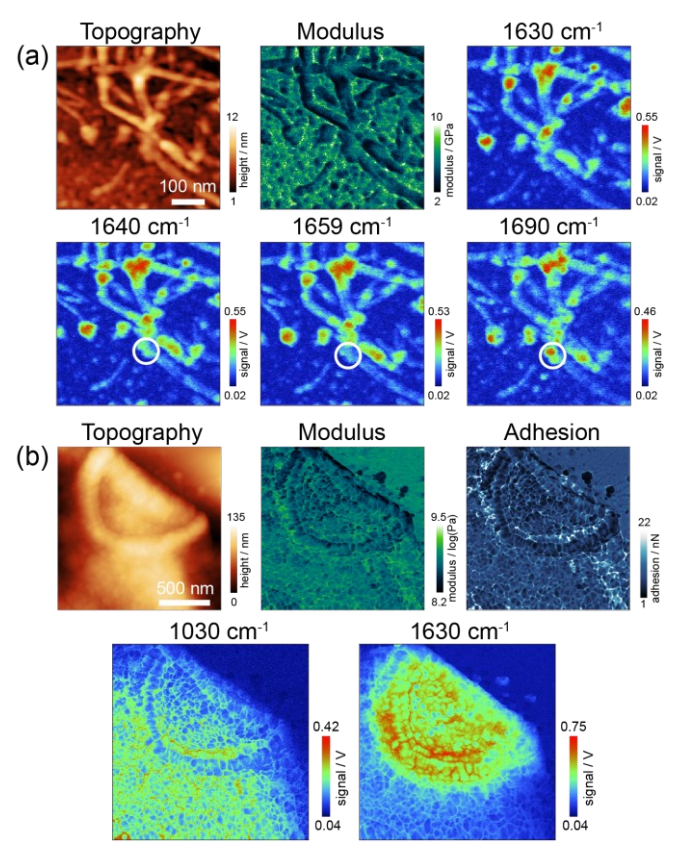


Fig. 11 PFIR images and spectra of fine and ultrafine indoor-collected aerosol particles. (a) Topography, adhesion, logarithmic of the modulus, and PFIR images at 1660 cm<sup>-1</sup> of a fine aerosol particle collected with filtration of a surgical mask in a local grocery store. Point spectra were obtained from the PFIR spectroscopy measurement at two locations marked in the topography image. (b) Topography, adhesion, together with PFIR images at 1725 cm<sup>-1</sup> and 1660 cm<sup>-1</sup> of an irregular-shaped aerosol particle collected without filtration of a mask in a residential house. Point spectra were acquired at two locations as marked in the topography image. The white arrow in the PFIR image at 1725 cm<sup>-1</sup> indicates an ultrafine aerosol particle. The spectra of location 1 in both (a) and (b) were vertically offset by 0.5 AU for clarity. Reproduced from Ref. 51 with permission from American Chemical Society, copyright 2021.



**Fig.12** PFIR results on FapC amyloid fibrils and budding sites of zymosan particles. (a) Topography, modulus, and PFIR images at 1630 cm<sup>-1</sup>, 1640 cm<sup>-1</sup>, 1659 cm<sup>-1</sup>, and 1690 cm<sup>-1</sup> of FapC fibrils. The white circles mark a fiber terminal that shows different IR responses when tuning IR frequencies. Adapted from Ref. 60 with permission from Society of Photo-Optical Instrumentation Engineers (SPIE), copyright 2020. (b) Topography, modulus, adhesion, and PFIR images at 1030 cm<sup>-1</sup> and 1630 cm<sup>-1</sup> of a zymosan bud scar. Adapted from Ref. 19 with permission from American Chemical Society, copyright 2020.

Apart from indoor fine and ultrafine aerosols, PFIR has also contributed to the intraparticle analysis of outdoor aerosols for assessment of air pollution and deduction of origins of airborne pollutants.<sup>41</sup> Not only organic species, but PFIR is also capable of detecting inorganic species such as sulfates, a product from the oxidation of SO<sub>2</sub> in vehicle exhaust.<sup>41</sup> Overall, combined with field studies and statistical analysis, PFIR microscopy is expected to provide hints on the sources and transformation of individual aerosol particles through the correlative study of chemical and mechanical properties, thus complementing existing techniques for aerosol research.

# 3.3. Probing protein secondary structures and heterogeneity of zymosan

Amyloids are misfolded protein aggregates and are known to be associated with many neurodegenerative disorders such as Alzheimer's and Parkinson's diseases.  $^{52,\,53}$  The formation of amyloid fibrils has been extensively studied, and the driving force is believed to be the folding of peptides with secondary structure in the form of  $\beta$ -sheet.  $^{54,\,55}$  Hence, the amount of  $\beta$ -sheet structure is a direct indication of the formation stage of amyloid fibrils. FTIR, Raman spectroscopy, and circular dichroism spectroscopy have been deployed to study the conformation of amyloids.  $^{56,\,57}$  However, the structural information derived from these methods is diffraction-

limited and reflects only an average of bulk samples. Superresolution fluorescence techniques have provided insights for *in situ* nanoscale study of chemical compositions, but the necessity of labeling inevitably causes potential interference to normal cells or protein dynamics. Therefore, we seek help from PFIR microscopy for a high-resolution and label-free method to build a correlation between amyloid formation and structural conformation change of single amyloid fibrils.

Amide I bond has a broad resonance peak in IR spectra and contains contributions from absorptions of various secondary structures. α-helices and β-sheets are two predominant secondary structures of polypeptides, of which the main absorption peaks center at 1640 – 1660 cm<sup>-1</sup> and 1690 cm<sup>-1</sup>, respectively.<sup>58</sup> FapC fibrils, which are functional amyloid proteins mainly found in biofilms of Enterobacteriaceae and Pseudomonas,59 have been studied by PFIR.<sup>60</sup> In Figure 12a, spherical oligomers, short amyloid protofibrils, and long mature amyloid fibrils are all observed. PFIR mapping at several frequencies also unveils the heterogeneous distribution of αhelices and β-sheets. Interestingly, a stronger response at 1690 cm<sup>-1</sup> is observed at the fibril terminal marked by the white circle. This phenomenon reveals that β-sheets are the major structural component at this location, suggesting its likely being at the stage of forming mature fibrils. We believe that if combined with statistical analysis on a large number of fibrils, PFIR will help construct the correlation between amyloid formation stage and relative amount of β-sheet structure of single fibrils, thus shedding light on the pathological study of protein misfolding diseases.

Another practical application of PFIR in biological samples is to identify nanoscale heterogeneous compositional distribution on yeast cell wall particles. 19 The yeast cell wall is a sturdy structure that plays a crucial role in determining cell shapes and protecting the cell from osmotic pressure caused by environment. 61, 62 The yeast cell wall particles, often known as zymosan particles, are extracted from Saccharomyces cerevisiae and rich in β-glucan and protein. Zymosan particles principally perform innate immune recognition and inflammatory induction towards microbes and have been treated as a model system for ages of microbial immunology. 63 Together with nanoscale mechanical properties, chemical compositions around a budding area of zymosan particles are revealed by PFIR in Figure 12b. The observed semicircle protruding area in Figure 12b is a bud scar left from the fracture of cell walls during division. PFIR images at 1030 cm<sup>-1</sup> and 1630 cm<sup>-1</sup> reveal the distribution of polysaccharides and protein inside and outside bud scars of the zymosan particles. A pronounced enrichment of proteins is found inside of bud scars, consistent with the published reports that proteins are recruited to the sites of bud scars during yeast budding. 64, 65 With the joint investigation of super-resolution fluorescence microscopy, the surface heterogeneity of the zymosan particle revealed by PFIR was shown to play roles in the heterogeneous recruitment of receptors on immune cell membranes.19

### 3.4. Study of geochemical properties of kerogen in oil shale rocks

The strength of PFIR microscopy shines in fossil fuel-related research as well. Encapsulated in the inorganic matrix of oil shale rocks, kerogen is one of the most abundant sources of hydrocarbons. 66-68 Scientists have made countless efforts in deepening the understanding of kerogen formation, evolution, and transformation

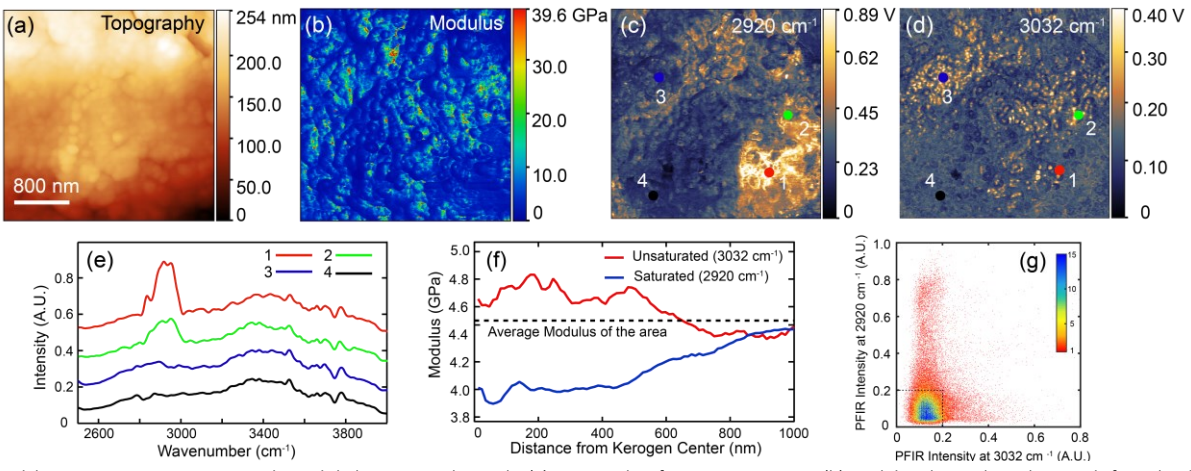


Fig. 13 Multimodal PFIR measurements on an Eagle Ford shale source rock sample. (a) Topography of a 3 μm × 3 μm area. (b) Modulus obtained simultaneously from the shale sample. (c-d) PFIR images at 2920 cm<sup>-1</sup> and 3032 cm<sup>-1</sup>. (e) PFIR spectra acquired from locations 1-4 as marked in (c) and (d). (f) The correlation between chemical identities and mechanical properties. Averaged modulus of surrounding matrix is plotted as a function of the distance from the hydrocarbons for both unsaturated and saturated channels. (g) A heatmap of normalized PFIR signal intensity for the determination of aromaticity, generated by plotting the correlated PFIR signals at 2920 cm<sup>-1</sup> with those at 3032 cm<sup>-1</sup> for each pixel. Reproduced from Ref. 18 with permission from American Chemical Society, copyright 2019.

to improve the efficiency of energy production.<sup>69-71</sup> At present, most characterization and modeling are based on macroscopic properties of kerogen, and the nanoscale geophysical and geochemical features are often omitted due to technical limitations. As a nanoscale tool, PFIR microscopy is exploited to unveil the nanoscale anisotropy as well as aromaticity and maturity of kerogen in oil shale rocks.<sup>18</sup>

Oil shale source rocks were received from the Eagle Ford shale play in southwest Texas and went through pulverization and mechanical press to form flat pellets. The multimodal PFIR results are demonstrated in Figures 13a-d, including mapping of the distributions of unsaturated hydrocarbons (3032 cm<sup>-1</sup>) and saturated hydrocarbons (2920 cm<sup>-1</sup>) along with modulus information. Point spectra at multiple locations are also shown in Figure 13e, which is consistent with the relative signal intensity in IR mapping. A noticeable correlation between mechanical and chemical properties is observed, where saturated hydrocarbons have a lower surrounding modulus while unsaturated species are more correlated with a higher surrounding modulus (Figure 13f). This finding is understandable because unsaturated moieties have higher densities than saturated moieties. High local pressure from the surrounding inorganic matrix favors the production of unsaturated hydrocarbons from saturated hydrocarbons in the cooking process over millions of years.<sup>72, 73</sup> Furthermore, the differentiated IR responses of saturated and unsaturated species allow the determination of in situ aromaticity of kerogen, represented by the relative amount of unsaturated moieties of hydrocarbons (shown in Figure 13g). With the feasibility of simultaneous retrieval of mechanical and chemical information, PFIR is expected to provide insights into detailed geochemical models and help understand the origin and evolution of kerogen in oil shale.

# 4. Applications of Liquid-phase PFIR

### 4.1. Liquid-phase PFIR in revealing phonon polaritons in water

Mid-IR PhPs of *h*-BN thin films have been extensively characterized by s-SNOM in the air, enabling a wide range of miniature photonic circuits/devices applications. On the flip side, the light-squeezing capability of PhPs also holds great promises for in-liquid nanoscale

photonics and chemical sensing. The excitation and detection of PhPs in liquids *in situ* would be ideal for such endeavors and facilitate the development of polaritonic materials and structures workable in various environments.

PhP patterns in the aqueous phase were revealed by liquid-phase PFIR microscopy for the first time.  $^{23}$  Figures 14a-b display Liquid-phase PFIR images of a thin  $h^{-10}$ BN edge with a 70-nm thickness in water. As expected, fringe patterns parallel to the edge were observed. Changing the incident wavelengths shifts the periodicity of the fringe pattern (Figure 14c), which is caused by varying momentum of tip-launched PhPs. In Figure 14d, a close examination of PhP patterns was conducted by plotting the energy-momentum dispersion relation of  $h^{-10}$ BN PhPs. The result aligns well with theoretical calculation but differs from measured PhPs in air. Such

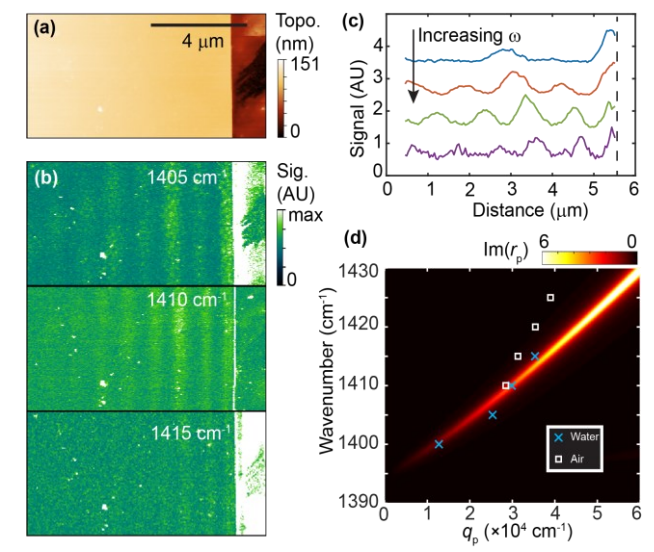


**Fig. 14** Liquid-phase PFIR in imaging phonon polaritons in water. (a) Topography of an edge of an  $h^{-10}$ BN flake in water. (b) Liquid-phase PFIR images at 1405 cm<sup>-1</sup>, 1410 cm<sup>-1</sup>, and 1415 cm<sup>-1</sup> incident frequencies. Fringe patterns parallel to the edge are revealed. (c) Signal profiles of fringe patterns extracted from Liquid-phase PFIR images. The black arrow shows the direction of increasing frequency from 1400 cm<sup>-1</sup>, 1410 cm<sup>-1</sup>, 1415 cm<sup>-1</sup>, to 1420 cm<sup>-1</sup>, and the vertical dashed curve shows the edge position. (d) Calculated dispersion relation (represented by the imaginary part of the reflectivity,  $Im(r_p)$ , using a false-color map) of  $h^{-10}$ BN in water overlaid with experiment results (crosses for results in water, squares for results in the air). Adapted from Ref. 23 with permission from American Chemical Society, copyright 2020.

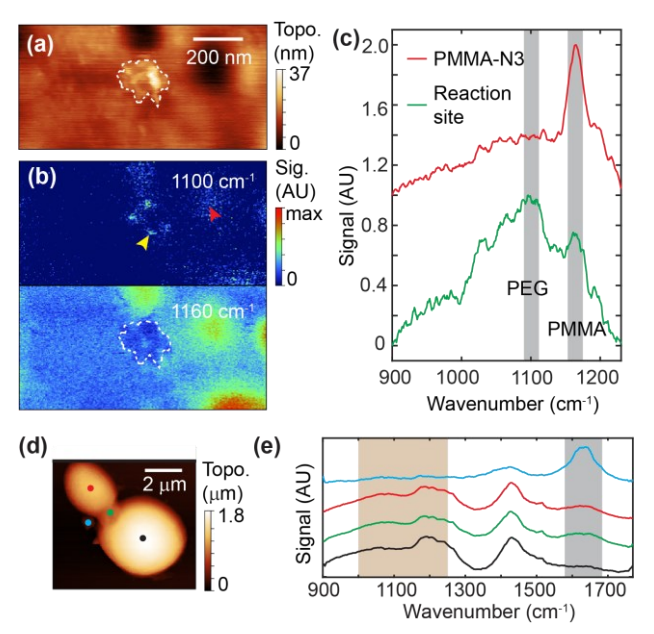


**Fig.15** Liquid-phase PFIR in imaging chemical reactions and biological samples. (a) Topography of a PMMA-N3 domain in PS:PMMA-N3 polymer blend film in the aqueous solution. A protrusion area (indicated by the white dashed enclosure) is observed after the click reaction. (b) Liquid-phase PFIR images at  $1100\,\mathrm{cm^{-1}}$  (PEG) and  $1160\,\mathrm{cm^{-1}}$  (PMMA-N3). (c) Point spectra collected from a hot spot (indicated by a yellow arrowhead in (b)) and the unreacted PMMA-N3 domain (indicated by a red arrowhead in (b)). Two grey shaded areas indicate PEG and PMMA bands. (d) Topography of two zymosan particles in heavy water. (e) Four-point spectra collected from four spots indicated by color dots in (d). IR absorption bands of polysaccharides and amides are indicated by brown and grey shaded areas, respectively. Adapted from Ref. 20 with permission from American Chemical Society, copyright 2021.

differences should be considered when designing polaritonic devices in different working conditions. These results demonstrate that PhPs can also be excited and photothermally detected in the h-BN/water interface, enabling liquid-phase PFIR as a useful tool to characterize nano-polaritonic devices in liquid conditions.

# 4.2. Liquid-phase PFIR in monitoring in situ click chemistry reactions

One of the most common routes used in click chemistry is coppercatalyzed azide-alkyne cycloaddition (CuAAC). In CuAAC, the presence of Cu(I) can catalyze the cycloaddition between azide and alkyne groups.<sup>74</sup> The ability to spatially resolve locations of reaction sites on heterogeneous substrates can offer detailed insights into the site-specific reactivity at the nanoscale.

Liquid-phase PFIR has been utilized to locate and monitor the reaction sites of CuAAC at a polymer/liquid interface. The polymer film used in this experiment contains  $\omega$ -azide-terminated PMMA (PMMA-N<sub>3</sub>, MW: 1000), and the other alkyne-containing reactant was alkyne-functionalized biotin through polyethylene glycol chains (biotin-PEG4-alkyne). The working solution was prepared by dissolving 7 mM biotin-PEG4-alkyne in water, with the addition of 1 mM CuSO<sub>4</sub> and 7 mM sodium L-ascorbate (C<sub>6</sub>H<sub>7</sub>NaO<sub>6</sub>) to generate Cu(I) species as catalysts. To initialize the CuAAC reaction, the solution was added to immerse the polymer surface. Based on distinctive IR absorptions of PEG (1100 cm $^{-1}$ ) and PMMA-N<sub>3</sub> (1160 cm $^{-1}$ ), liquid-phase PFIR could pinpoint nanoscale domains where CuAAC

happened. Figure 15a displays the topography of one small area of PMMA-N<sub>3</sub> film. After 24 hours of the reaction, PFIR images at 1100 cm<sup>-1</sup> and 1160 cm<sup>-1</sup> were obtained and shown in Figure 15b. A tiny, protruded area with the size of ~200 nm could be observed on the PMMA-N<sub>3</sub> domain. There are four hot spots around this protruded area in the PEG map at 1100 cm<sup>-1</sup>, while these spots remain dark in the PMMA-N<sub>3</sub> map at 1160 cm<sup>-1</sup>. The appearance of PEG signals in the 1100 cm<sup>-1</sup> map indicates that the click reaction has taken place at those hot spots. The existence of CuAAC products at these four spots was further confirmed by comparing the point spectrum collected from one of the four hot spots to that from the unreacted PMMA-N<sub>3</sub> surface (Figure 15c). IR absorptions at both 1100 cm<sup>-1</sup> and 1160 cm<sup>-1</sup> indicate that these spots are composed of PMMA-PEGbiotin molecules formed from the click chemistry. A detection level of  $1.2 \times 10^3$  biotin-PEG-alkyne molecules is estimated by analyzing the volume of one reaction site. This zeptomolar sensitivity is in accordance with standard PFIR.14

#### 4.3. Liquid-phase PFIR in investigating yeast budding site

Zymosan particles derived from the yeast *Saccharomyces cerevisiae* were adopted as examples to demonstrate the capability of liquid-phase PFIR microscopy to imaging biological cells. The chemical structure of dried zymosan particles in the air has already been investigated with standard PFIR (Figure 12b).  $^{19}$  When dried on substrates, zymosan particles tend to hold flattened disk-like shapes with heights of 200-300 nm, and their nucleoli will protrude prominently from the rest of the particle because of the shrinkage of the cell volume. However, the native shape of zymosan particles in physiological environments is ellipsoidal, enclosing nucleoli inside the particle. Liquid-phase PFIR in water could uncover chemical information of native zymosan particles, which is more relevant to immunomodulator applications in physiological environments.

The topography image of a pair of zymosan particles in heavy water is shown in Figure 15d. When in heavy water, the height of zymosan particles increased up to 1.8 µm. A septum was formed between two zymosan particles, indicating the two particles were from two yeast cells in the middle of the budding process. After budding, a budding scar will form at the budding site of each cell. Point spectra were collected from four different locations nearby to study the chemical composition around the budding site. In Figure 15e, IR signatures of polysaccharides were observable as expected on the surface of zymosan particles and septum; On a cluster close to the budding site, however, a prominent amid I band around 1630 cm<sup>-1</sup> appeared while the polysaccharide signal diminished. The variations in point IR spectra clearly indicate the presence of proteins around the budding site, which may take part in the chitin synthesis during the yeast budding.75 This application showcases the biocompatibility of liquid-phase PFIR, which opens the door for more studies to probe bio mechanisms with unprecedented details in vivo.

# 5. Comparison of the PFIR microscopy among AFM-IR techniques

Among AFM-IR techniques, the PFIR microscopy has advantages and limitations. Table 1 summarizes the respective attributes of current

AFM-IR techniques, including the original contact mode PTIR, REINS/resonance enhanced AFM-IR, PiFM/tapping mode AFM-IR, and the PFIR microscopy. The PFIR microscopy compares favorably in terms of spatial resolution, preservation of sample surface integrity, complementary mechanical measurement. The limitation of the PFIR microscopy, compared with sister AFM-IR method, is that the photothermal measurement only happens when the tip-sample is in dynamic contact, which reduces the upper limit of the duty cycle of photothermal signal generation. Consequently, the maximal possible measurement speed of the PFIR microscopy should be slower than that of PiFM or tapping mode AFM-IR. Another limitation is that the time domain gated detection requires software/hardware programming of data acquisition card (e.g., PXI-5122 National Instruments). Such an approach requires a level of expertise on programming, which means an entry barrier for chemists. In comparison, other AFM-IR methods can be done with frequency domain lock-in detection, which is simpler to implement with existing commercially available equipment.

A notable attribute of the PFIR microscopy is its adaptability with IR light sources with different repetition rates. While the signal of the PFIR microscopy benefits from IR sources with high repetition rates,

e.g., QCL at >100 kHz, the original single pulse PFIR microscopy works well with low-repetition-rate light sources, such as nanosecond IR OPO at 1 or 2 kHz repetition rate. The ability for PFIR to work with low-repetition-rate light sources while still providing high spatial resolution and preserving the sample integrity is advantageous for the PFIR microscopy to be integrated with currently popular kHz repetition rate laser systems, such as Ti:Sapphire or Yb:KGW laser amplifiers.

Compared with PiFM, the PFIR microscopy has a more straightforward signal interpretation, while offering comparable spatial resolutions. One possible signal generation mechanism for PiFM is the photo-induced dipole-dipole force model, <sup>10,76</sup> in parallel with photothermal modulated van der Waals force. A recent model of PiFM further attributes its signals the optomechanical damping origin when the tip and sample has a close distance but not in contact. <sup>77</sup> In contrast, the PFIR microscopy operates during the deterministic tip-sample contact with straightforward photothermal signal generation without the additional signal generation pathways of the PiFM. Such a simplicity of the PFIR is advantages for chemical analysis and quantification.

Table 1. Comparison of current AFM-IR techniques

|  | PTIR (original)                               | REINS/Resonance enhanced AFM-IR | PiFM/Tapping mode AFM-IR             | PFIR   |
|--|---|---------------------------------|--------------------------------------|--|
| Parent AFM mode                                | Contact mode                                  | Contact mode                    | Non-contact/tapping mode             | Peak force tapping mode  |
| Signal detection                               | Lock-in or Data acquisition card              | Lock-in                         | Lock-in                              | Data acquisition card  |
| Signal origin                                  | Photothermal                                  | Photothermal                    | Photo-induced force or photothermal  | Photothermal   |
| Sample scratch                                 | Possible                                      | Possible                        | Low chance                           | Low chance   |
| Typical spatial resolution                     | 50 ~ 100 nm                                   | 25 ~ 50 nm                      | ~ 10 nm                              | 6 ~ 10 nm  |
| Other complimentary material property channels | Mechanical property through contact resonance | Not available                   | Not available                        | Quantitative mechanical property<br>by PeakForce QNM<br>Surface potential with PFIR-KPFM |
| Repetition rate of IR pulses                   | ~10 <sup>3</sup> Hz                           | ~10 <sup>5</sup> Hz             | 10 <sup>5</sup> ~ 10 <sup>6</sup> Hz | ~10³ for original PFIR<br>~ 10⁵ Hz for multi-pulse PFIR                                  |

# 6. Conclusions and outlook

microscopy enables a general platform nanospectroscopy based on photothermal detections. For example, the same signal generation and detection mechanism could be readily extended into other frequency regimes without compromising spatial resolution. The utilization of near infrared (NIR) radiation would provide an easy imaging modality for aqueous phase, as the NIR photon penetrates well in water. Implementing UV and visible light sources with PFIR-type microscopy shall provide chemical imaging based on the absorption from electronic excitations. The combination of far IR and THz light sources in PFIR microscopy will address the question of low-frequency vibrational/phonon modes and resolve charge carrier generation and dissipation. Photothermal detection in the THz regime would bypass the limitations on optical detection, which currently requires a complex apparatus based on electro-optical sampling.

The direct temporal domain mechanical detection of PFIR microscopy also provides the potential implementation of multiplexing detection. Further development from the dual-color PFIR microscopy may include more than two QCLs. For example, integrating three or more QCL sources in a multi-color PFIR microscopy would enable simultaneous multiplex IR nano-imaging at 10 nm spatial resolution.

Another possible development of the PFIR microscopy is to combine it with short-duration ultrafast laser pulses to achieve pump-probe nanoscopy in the time domain. For example, detecting the difference of photothermal response as a function of time delay between the pump and probe pulses would provide a route toward spatial-temporal nano-imaging, complementary to the current near-field s-SNOM approaches.<sup>78</sup> Further combination of the PFIR microscopy with broadband IR light pulse sequence could reach the much desired two-dimensional (2D) IR nanospectroscopy. The

combination of photothermal detection with currently well-developed 2D IR techniques may further elucidate the complex excited-state dynamics or mode coupling far below the spatial scale set by the optical diffraction limit. The compatibility of PFIR with low-repetition-rate femtosecond amplifiers suits well with these possible time-domain development.

As a nano-IR method, PFIR microscopy has potential in many research fields. The label-free chemical imaging by PFIR is suitable for detecting chemical reactions at air/solid surfaces or liquid/solid interfaces, particular with the implementation of dual-color PFIR. For example, if PFIR microscopy is implemented at a high-temperature condition, the adsorbed reactant and product molecules on a nanoto micro-scale catalyst can be individually monitored *in situ*. The possible extension of the PFIR microscopy into the low-temperature operation may also provide insights into the polaritons of the 2D material. Compared with s-SNOM, a low-temperature PFIR microscope would have a simpler optical design and a smaller footprint, which are more flexible for integrating low-temperature cryostat with the AFM.

Enabled by the emergence of pulsed force mode, the performance ceiling of PFIR microscopy is intrinsically linked to the improvement of the PFT as well. The upper ceiling on the operational speed of the PFIR microscopy stems from the operating frequency of the PFT mode. If the PFT frequency can be further improved above the state-of-the-art of 8 kHz, the scan speed of PFIR microscopy can be improved accordingly, which may enable the hyperspectral mode of PFIR—collecting spectrum at every spatial location during scans. A specially designed AFM probe would also need to be developed for high-speed PFIR microscopy. An optimal AFM cantilever for PFIR should have a high Q-factor for contact resonance oscillation and a low Q-factor for fundamental mechanical resonance. The high Qfactor for contact resonance can increase the signal strength. In contrast, the low Q-factor for fundamental mechanical resonance can avoid residual cantilever oscillation after the detachment of the AFM tip. Furthermore, a geometrically tailored AFM tip should also improve spatial resolution and signal strength. Ideally, such a tip should maximally enhance the IR field while minimizing the contact area with the sample to achieve both high signal strength and high spatial resolution. This feature may be delivered by functionalizing IR plasmon/polariton-active AFM tip with small nanoscopic metal particles.

### **Conflicts of interest**

There are no conflicts to declare.

# **Acknowledgments**

X. G. X. would like to thank the support from Beckman Young Investigator Award from the Arnold and Mabel Beckman Foundation and the Sloan Research Fellowship from the Alfred P. Sloan Foundation, and Camille Dreyfus Teacher-Scholar Award from the Camille and Henry Dreyfus Foundation. L. W., H. W., and X. G. X. would also like to thank the support from the National Science Foundation, award number CHE 1847765

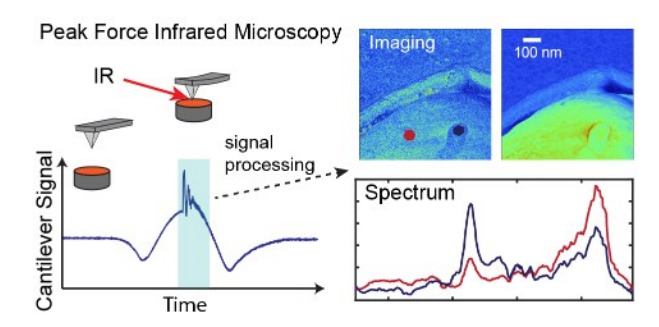
### References

- 1. E. Abbe, Archiv für Mikroskopische Anatomie, 1873, **9**, 413-468.
- 2. B. Bhushan, B. Bhushan and Baumann, *Springer handbook of nanotechnology*, Springer, 2007.
- 3. X. Chen, D. Hu, R. Mescall, G. You, D. Basov, Q. Dai and M. Liu, *Advanced Materials*, 2019, **31**, 1804774.
- 4. S. Kawata and V. M. Shalaev, Tip enhancement, Elsevier, 2011.
- A. Dazzi and C. B. Prater, Chemical Reviews, 2017, 117, 5146-5173.
- 6. M. S. Anderson, Applied Spectroscopy, 2000, 54, 349-352.
- 7. A. Dazzi, R. Prazeres, F. Glotin and J. M. Ortega, *Optics Letters*, 2005, **30**, 2388-2390.
- 8. D. Kurouski, A. Dazzi, R. Zenobi and A. Centrone, *Chemical Society Reviews*, 2020, **49**, 3315-3347.
- F. Lu, M. Jin and M. A. Belkin, *Nature Photonics*, 2014, 8, 307-312.
  J. Jahng, E. O. Potma and E. S. Lee, *Analytical Chemistry*, 2018, 90, 11054-11061.
- 11. C. Mayet, A. Dazzi, R. Prazeres, F. Allot, F. Glotin and J. M. Ortega, *Optics Letters*, 2008, **33**, 1611-1613.
- 12. M. Jin, F. Lu and M. A. Belkin, *Light: Science & Applications*, 2017, **6**, e17096-e17096.
- 13. G. Ramer, F. S. Ruggeri, A. Levin, T. P. J. Knowles and A. Centrone, *ACS Nano*, 2018, **12**, 6612-6619.
- 14. L. Wang, H. Wang, M. Wagner, Y. Yan, D. S. Jakob and X. G. Xu, *Science Advances*, 2017, **3**, e1700255.
- 15. A. Rosa-Zeiser, E. Weilandt, S. Hild and O. Marti, *Measurement Science and Technology*, 1997, **8**, 1333.
- 16. B. Pittenger, N. Erina and C. Su, *Application Note Veeco Instruments Inc*, 2010, **1**, 1-11.
- 17. K. Xu, W. Sun, Y. Shao, F. Wei, X. Zhang, W. Wang and P. Li, Nanotechnology Reviews, 2018, 7, 605-621.
- 18. D. S. Jakob, L. Wang, H. Wang and X. G. Xu, *Anal. Chem.*, 2019, **91**, 8883-8890.
- 19. W. Li, H. Wang, X. G. Xu and Y. Yu, *Langmuir*, 2020, **36**, 6169-6177.
- 20. H. Wang, J. M. González-Fialkowski, W. Li, Q. Xie, Y. Yu and X. G. Xu, *Analytical Chemistry*, 2021, **93**, 3567-3575.
- 21. L. Wang, M. Wagner, H. Wang, S. Pau-Sanchez, J. Li, J. H. Edgar and X. G. Xu, *Advanced Optical Materials*, 2020, **8**, 1901084.
- 22. H. Wang, L. Wang, E. Janzen, J. H. Edgar and X. G. Xu, *Analytical Chemistry*, 2021, **93**, 731-736.
- 23. H. Wang, E. Janzen, L. Wang, J. H. Edgar and X. G. Xu, *Nano Letters*, 2020, **20**, 3986-3991.
- 24. H. Wang, Q. Xie, Y. Zhang and X. G. Xu, *The Journal of Physical Chemistry C*, 2021, **125**, 8333-8338.
- 25. Q. Xie, J. Wiemann, Y. Yu and X. G. Xu, *Analytical Chemistry*, 2022, **94**, 1425-1431.
- 26. D. S. Jakob, H. Wang, G. Zeng, D. E. Otzen, Y. Yan and X. G. Xu, *Angewandte Chemie International Edition*, 2020, **59**, 16083-16090.
- 27. B. V. Derjaguin, V. M. Muller and Y. P. Toporov, *Journal of Colloid and Interface Science*, 1975, **53**, 314-326.
- 28. C. Su, Microscopy and Microanalysis, 2010, **16**, 364-365.
- 29. G. J. Verbiest and M. J. Rost, *Ultramicroscopy*, 2016, **171**, 70-76.
- 30. B. Pittenger, N. Erina and C. Su, in *Nanomechanical Analysis of High Performance Materials*, ed. A. Tiwari, Springer Netherlands, Dordrecht, 2014, DOI: 10.1007/978-94-007-6919-9\_2, pp. 31-51.
- 31. B. Cappella, S. K. Kaliappan and H. Sturm, *Macromolecules*, 2005, **38**, 1874-1881.
- 32. L. Holliday and J. Robinson, *Journal of Materials Science*, 1973, **8**, 301-311.
- 33. Y. Fei, in Mineral Physics & Crystallography, 1995, pp. 29-44.

- 34. L. Wang, M. Wagner, H. Wang, S. Pau Sanchez, J. Li, J. H. Edgar and X. G. Xu, *Advanced Optical Materials*, 2020, **8**, 1901084.
- 35. F. M. Mirabella, *Internal reflection spectroscopy: theory and applications*, CRC Press, 1992.
- 36. B. T. O'Callahan, K.-D. Park, I. V. Novikova, T. Jian, C.-L. Chen, E. A. Muller, P. Z. El-Khoury, M. B. Raschke and A. S. Lea, *Nano Letters*, 2020, **20**, 4497-4504.
- 37. E. Pfitzner and J. Heberle, *The Journal of Physical Chemistry Letters*, 2020, **11**, 8183-8188.
- 38. D. Virmani, A. Bylinkin, I. Dolado, E. Janzen, J. H. Edgar and R. Hillenbrand, *Nano Letters*, 2021, **21**, 1360-1367.
- 39. J. Tamayo, A. D. L. Humphris, R. J. Owen and M. J. Miles, *Biophysical Journal*, 2001, **81**, 526-537.
- 40. D. S. Jakob, H. Wang and X. G. Xu, *ACS Nano*, 2020, **14**, 4839-4848.
- 41. L. Wang, D. Huang, C. K. Chan, Y. J. Li and X. G. Xu, *Chemical Communications*, 2017, **53**, 7397-7400.
- 42. C. Gusenbauer, D. S. Jakob, X. G. Xu, D. V. Vezenov, É. Cabane and J. Konnerth, *Biomacromolecules*, 2020, **21**, 4244-4252.
- 43. C. Gusenbauer, T. Nypelö, D. S. Jakob, X. G. Xu, D. V. Vezenov, S. Asaadi, H. Sixta and J. Konnerth, *International Journal of Biological Macromolecules*, 2020, **165**, 2520-2527.
- 44. Y. Li, J. Ding, C. Liang, X. Zhang, J. Zhang, D. S. Jakob, B. Wang, X. Li, H. Zhang, L. Li, Y. Yang, G. Zhang, X. Zhang, W. Du, X. Liu, Y. Zhang, Y. Zhang, X. Xu, X. Qiu and H. Zhou, *Joule*, 2021, **5**, 3154-3168.
- 45. N. Li, X. Niu, L. Li, H. Wang, Z. Huang, Y. Zhang, Y. Chen, X. Zhang, C. Zhu, H. Zai, Y. Bai, S. Ma, H. Liu, X. Liu, Z. Guo, G. Liu, R. Fan, H. Chen, J. Wang, Y. Lun, X. Wang, J. Hong, H. Xie, S. Jakob Devon, G. Xu Xiaoji, Q. Chen and H. Zhou, *Science*, 2021, **373**, 561-567.
- 46. P. Chen, Y. Liu, X. Hu, X. Liu, E.-M. You, X. Qian, J. Chen, L. Xiao, L. Cao and X. Peng, *Nano Research*, 2020, **13**, 3151-3156.
- 47. K. Ho, K. S. Kim, S. de Beer and G. C. Walker, *Langmuir*, 2021, **37**, 12723-12731.
- 48. C. I. Davidson, R. F. Phalen and P. A. Solomon, *Aerosol Science and Technology*, 2005, **39**, 737-749.
- 49. S. Tang, Y. Mao, R. M. Jones, Q. Tan, J. S. Ji, N. Li, J. Shen, Y. Lv, L. Pan and P. Ding, *Environment international*, 2020, **144**, 106039.
- 50. S. J. Silva, J. Nascimento, W. Reis, C. Silva, P. Silva, R. Mendes, A. Mendonca, B. Santos, J. Magalhaes and A. Kohl, *medRxiv*, 2021.
- 51. J. M. González-Fialkowski, L. Wang, Y. J. Li and X. G. Xu, *Analytical Chemistry*, 2021, DOI: 10.1021/acs.analchem.1c03659.
- 52. J. A. Hardy and G. A. Higgins, Science, 1992, 256, 184-186.
- 53. H. A. Lashuel, D. Hartley, B. M. Petre, T. Walz and P. T. Lansbury, *Nature*, 2002, **418**, 291-291.
- 54. C. Blake and L. Serpell, *Structure*, 1996, **4**, 989-998.
- 55. M. S. Dueholm, S. V. Petersen, M. Sønderkær, P. Larsen, G. Christiansen, K. L. Hein, J. J. Enghild, J. L. Nielsen, K. L. Nielsen and P. H. Nielsen, *Molecular microbiology*, 2010, **77**, 1009-1020.
- 56. M. Fändrich, M. A. Fletcher and C. M. Dobson, *Nature*, 2001, **410**, 165-166.
- 57. M. R. Nilsson, Methods, 2004, 34, 151-160.
- 58. Z. Ganim, H. S. Chung, A. W. Smith, L. P. DeFlores, K. C. Jones and A. Tokmakoff, *Accounts of chemical research*, 2008, **41**, 432-441.
- 59. M. S. Dueholm, D. Otzen and P. H. Nielsen, *PLoS One*, 2013, **8**, e76630.
- 60. L. Wang, G. Zeng, G. Walker and X. Xu, *Peak force infrared microscopy for label-free chemical imaging at sub 10 nm spatial resolution*, SPIE, 2020.
- 61. M. Osumi, Micron, 1998, 29, 207-233.
- 62. S. M. Bowman and S. J. Free, *Bioessays*, 2006, **28**, 799-808.
- 63. M. Novak and V. Vetvicka, *Journal of Immunotoxicology*, 2008, **5**, 47-57.

- 64. T. Sumita, T. Yoko-o, Y.-i. Shimma and Y. Jigami, *Eukaryotic Cell*, 2005, **4**, 1872-1881.
- 65. E. Rolli, E. Ragni, J. Calderon, S. Porello, U. Fascio and L. Popolo, *Molecular biology of the cell*, 2009, **20**, 4856-4870.
- 66. L. Cueto-Felgueroso and R. Juanes, *Proceedings of the National Academy of Sciences*, 2013, **110**, 19660-19661.
- 67. M. Vandenbroucke and C. Largeau, *Organic Geochemistry*, 2007, **38**. 719-833.
- 68. T.-Y. Wang, S.-C. Tian, Q.-L. Liu, G.-S. Li, M. Sheng, W.-X. Ren and P.-P. Zhang, *Petroleum Science*, 2021, **18**, 565-578.
- 69. P. R. Craddock, K. D. Bake and A. E. Pomerantz, *Energy & Fuels*, 2018, **32**, 4859-4872.
- 70. D. Lai, J.-H. Zhan, Y. Tian, S. Gao and G. Xu, Fuel, 2017, **199**, 504-
- 71. X. Wang and Y.-P. Zhao, Fuel, 2020, 278, 118264.
- 72. K. S. Okiongbo, A. C. Aplin and S. R. Larter, *Energy & fuels*, 2005, **19**, 2495-2499.
- 73. Y. Zeng and C. Wu, Fuel, 2007, 86, 1192-1200.
- 74. J. E. Hein and V. V. Fokin, *Chemical Society Reviews*, 2010, **39**, 1302-1315.
- 75. E. Cabib and A. Durán, *Journal of Biological Chemistry*, 2005, **280**, 9170-9179.
- 76. J. Jahng, E. O. Potma and E. S. Lee, *Proceedings of the National Academy of Sciences*, 2019, **116**, 26359.
- 77. M. A. Almajhadi, S. M. A. Uddin and H. K. Wickramasinghe, *Nature Communications*, 2020, **11**, 1-9.
- 78. M. Wagner, Z. Fei, A. S. McLeod, A. S. Rodin, W. Bao, E. G. Iwinski, Z. Zhao, M. Goldflam, M. Liu and G. Dominguez, *Nano Letters*, 2014, 14, 894-900.

# ToC Graphic



Peak force infrared (PFIR) microscopy is an atomic force microscopy based infrared microscopy with multimodal characterization capabilities. The PFIR microscopy allows ~10 nm spatial resolution chemical imaging in both the air and liquid phases.